Cover Statement

Viscosity of anhydrous and hydrous peridotite melts

Danilo Di Genova[1,2], Dmitry Bondar[1], Alessio Zandonà[3,4,*], Pedro Valdivia[1], Raschid Al-Mukadam[5], Hongzhan Fei[1], Anthony C. Withers[1], Tiziana Boffa Ballaran[1], Alexander Kurnosov[2], Catherine McCammon[1], Joachim Deubener[5], Tomoo Katsura[1]

[1]Bayerisches Geoinstitut, University of Bayreuth, Universitätsstraße 30, 95440, Bayreuth, Germany
[2]Institute of Environmental Geology and Geoengineering, National Research Council of Italy, Rome, Italy
[3]CNRS, CEMHTI UPR3079, Univ. Orléans, F-45071 Orléans, France
[4]Friedrich-Alexander-Universität Erlangen-Nürnberg, Department of Materials Science (Glass and Ceramics), Martensstr. 5, 91058 Erlangen, Germany
[5]Institute of Non-metallic Materials, Clausthal University of Technology, Zehntnerstraße 2a, D-38678 Clausthal-Zellerfeld, Germany

*Corresponding authors: alessio.zandona@fau.de

Abstract

The melt viscosity (η) of anhydrous and hydrous peridotite was investigated using a multipronged approach combining micropenetration viscometry, conventional DSC, flash DSC and Brillouin spectroscopy. Raman spectroscopy measurements were used to verify the absence of crystallization and/or degassing during high-temperature measurements of these extremely reactive glasses and melts, ensuring that the data corresponded to the crystal-free melt viscosity. Based on the experimental data, an accurate description of the viscosity of peridotite melts over thirteen orders of magnitude (from T_g to $\eta \approx 10^{-1}$ Pa s) is provided in a broad range of compositions and oxidation states. Since empirical models predict viscosities that can significantly deviate from measured data to varying degrees, a new model was developed for the temperature- and H_2O-dependent viscosity of peridotite melts (up to 12 mol% H_2O content).

Keywords: peridotite melt; viscosity; glass transition; calorimetry; Brillouin spectroscopy

1. Introduction

Magmatic activity is a daily occurrence on Earth (Loughlin et al., 2015). The lavas that are produced have a wide variety of compositions (Keller and Krafft, 1990; Lipman and Mullineaux, 1981; Mahood and Hildreth, 1986; Pirrung et al., 2003; Sigurdsson et al., 1982; Sigurdsson and Carey, 1989; Walker et al., 1984), extending from extremely SiO_2-rich rhyolites to carbonatites. Chemical composition (including volatile content) ultimately determines the intrinsic viscoelastic properties of magmas and the tendency to partially crystallize and degas, so that it represents a crucial parameter controlling the eruptive styles of volcanoes (Gonnermann and Manga, 2013). Among those parameters that govern both magma transport from the reservoir to the volcanic vent and eruptive style, viscosity is arguably the most important (Cassidy et al., 2018; Di Genova et al., 2017a). Indeed, volcanologists have long pursued the experimental investigation of melt viscosity as a function of temperature and composition (e.g., Ishibashi and Sato, 2007; Kolzenburg et al., 2018; Whittington et al., 2009), as well as its subsequent numerical modelling by different approaches including classical linear regression and machine learning (Giordano et al., 2008; Hui and Zhang, 2007; Langhammer et al., 2022). The extent and quality of the dataset used to develop these models directly affect the reliability of their predictions, so that one should strive for a detailed experimental exploration of the largest possible compositional landscape. Unfortunately, there are undeniable experimental challenges related to the viscosity measurements of volcanic melts (or their synthetic analogs), namely: (i) their undercooling-driven tendency to crystallize, which typically limits concentric-cylinder low-viscosity ($\sim 10^4$–10^{-2} Pa s) determinations (e.g., Kolzenburg et al., 2018) to superliquidus temperatures and only mild undercooling; (ii) the prompt degassing of volatile-bearing melts at ambient pressure, which can be only overcome through falling-sphere experiments and the application of confining pressure (e.g., Liebske et al., 2005), with significant technical difficulties; (iii) the limited glass-forming ability of volcanic compositions, since glassy samples are necessary for high-viscosity (10^{12}–10^{6} Pa s) measurements by micropenetration (e.g., Di Genova et al., 2020b), parallel-plate deformation (e.g., Whittington et al., 2009), beam bending (e.g., Hagy, 1963) or fiber elongation (e.g., Taniguchi, 1992) viscometry. Moreover, even when the required glassy samples can be synthesized, their limited stability during high-temperature measurements has been repeatedly demonstrated by postmortem measurements using Raman spectroscopy and high-resolution imaging (Di Genova et al., 2020b, 2017a; Kleest et al., 2020; Liebske et al., 2003a; Scarani et al., 2022): nanocrystallization of Fe-Ti-oxides can affect sample homogeneity and alter the composition of the residual melt, preventing derivation of the crystal-free viscosity. As a consequence, currently available viscosity models (Giordano et al., 2008; Hui and Zhang, 2007; Langhammer et al., 2022) have been trained in a relatively restricted volcanological domain of temperature and chemistry, with questionable applicability to compositional extremes such as ultrabasic melts and very H_2O-rich matrices.

To overcome these limitations, we designed this work as a targeted investigation of melts that locate substantially outside the range of previously analyzed compositions, considering an unprecedented range of anhydrous and hydrous viscosities and testing the predictive performance of numerical viscosity models available in the literature (Giordano et al., 2008; Hui and Zhang, 2007; Langhammer et al., 2022). We therefore selected anhydrous and hydrous peridotite liquids: the viscosity of these materials was investigated only sporadically so far (Dingwell et al., 2004; Liebske et al., 2005) due to their extreme features, namely a SiO_2 content < 50 wt% that leads to extreme structural depolymerization and a very strong tendency to undercooling-driven crystallization. However, ultramafic liquids play a key role for our understanding of deep mantle dynamics and for planetary formation theories: the Earth is thought to have experienced a large degree of melting during planetary accretion, as well as after the giant impact that originated the Moon (e.g., Nakajima and Stevenson, 2015; Ohtani, 1985). The resulting peridotite magma oceans facilitated core formation through silicate-metal segregation (e.g., Li and Agee, 1996; Wade and Wood, 2005) and originated the atmosphere and hydrosphere through degassing (e.g., Karato et al., 2020; Sossi et al., 2020). Moreover, high-pressure experiments demonstrated that highly ultramafic and Mg-rich melts (such as picrites and kimberlites) could be formed at present by partial melting of peridotite in the upper and lower mantle (e.g., Fei, 2021; Kawamoto and Holloway, 1997; Mysen and Boettcher, 1975; Sinmyo et al., 2019), with far-reaching implications for the transport of incompatible elements such as hydrogen (Karato et al., 2020).

For the synthesis of anhydrous ultrabasic melts and glasses, we relied on aerodynamic levitation coupled with laser heating (Hennet et al., 2011; Weber, 2010) which facilitates glass formation by suppressing heterogeneous surface nucleation due to its containerless conditions; in the case of hydrous peridotite melts, we employed a recently developed rapid-quench multi-anvil technique (Bondar et al., 2021, 2020). Due to the occasionally very low amounts of available material (especially for hydrous samples), we studied melt viscosity using a multipronged experimental approach (see Section 1.1) carefully combining classical viscometry with standard and flash calorimetry and Brillouin spectroscopy, whose applicability is here tested and demonstrated to be successful also for such extreme compositions. On the whole, our results provide the first quantitative parameterization of peridotite melt viscosity as a function of temperature, overall composition (e.g., FeO_{tot}) and water content (up to 12 mol%).

1.1. Deriving and modelling melt viscosity

The experimental procedure applied in this work has been presented, tested and optimized in previous studies (Cassetta et al., 2021; Di Genova et al., 2020b; Scarani et al., 2022; Stabile et al., 2021); its cornerstones are briefly summarized here. We have demonstrated that the combination of calorimetry (DSC) and Brillouin spectroscopy (BLS) enables the modelling of melt viscosity as a function of temperature [$\eta(T)$] (Cassetta et al., 2021). We model $\eta(T)$ using the three-parameter MYEGA equation (Eq. 1) (Mauro et al., 2009b):

$$log_{10}\eta(T) = log_{10}\eta_\infty + (12 - log_{10}\eta_\infty)\frac{T_g}{T}exp\left[\left(\frac{m}{12-log_{10}\eta_\infty} - 1\right)\left(\frac{T_g}{T} - 1\right)\right] \qquad (1)$$

where $\log_{10}\eta_\infty$ is the viscosity at infinite temperature (Langhammer et al., 2021; Zheng et al., 2011), T_g is the glass transition temperature [$\eta(T_g) = 10^{12}$ Pa s] and m is the melt fragility (Eq. 2) (Angell, 1995):

$$m = \left.\frac{\partial log_{10}\eta}{\partial T_g/T}\right|_{T=T_g} \qquad (2)$$

The existence of a universal, chemically invariant limit of viscosity at infinite temperature constitutes a long-standing concept, already elaborated using other parameterizations such as the Adam-Gibbs (AG) or the Vogel–Fulcher–Tammann–Hesse (VFTH) equations (Persikov, 1991; Russell et al., 2003, 2002). For the MYEGA equation, this value was calibrated to $\log_{10}\eta_\infty = -2.93 \pm 0.3$ for silicate melts of volcanological and technological interest (Langhammer et al., 2021; Zheng et al., 2011). Notably, this value is close to the lowest viscosity values measured at high temperatures in silicate and carbonatite melts (Di Genova et al., 2016a; Dingwell et al., 2022; Dobson et al., 1996; Kono et al., 2014; Persikov et al., 2017; Stagno et al., 2018). By fixing this value, only T_g and m are required to parameterize $\log_{10}\eta(T)$.

The melt fragility m was derived spectroscopically from BLS measurements performed on glasses at room temperature (Cassetta et al., 2021) because this approach avoids the need to acquire viscosity data over an extended temperature range, which is challenging or impossible for poor glass-forming liquids (Di Genova et al., 2020b; Kleest et al., 2020; Liebske et al., 2003b; Richet et al., 1996; Scarani et al., 2022). Fragility m was obtained as (Eq. 3):

$$m = 43.429 \cdot \frac{K}{G} - 31.871 \qquad (3)$$

where K/G is the elastic moduli ratio calculated (Eq. 4) using the measured shear v_s and longitudinal v_p sound velocities (Cassetta et al., 2021):

$$\frac{K}{G} = \left(\frac{v_p}{v_s}\right)^2 - \frac{4}{3} \qquad (4)$$

For samples of sufficient size and exhibiting enough glass stability to be measured by DSC (here, anhydrous peridotite glasses), we derived T_g via DSC. The DSC approach to derive T_g builds on the relationship (Eq. 5) provided by (Scherer, 1984):

$$log_{10}\eta\left(T_f\right) = K - log_{10}(q_h) \qquad (5)$$

where q_h is the heating rate in K s^{-1} employed during the DSC measurement and T_f is the fictive temperature in Kelvin, at which the structure and properties (e.g., volume and enthalpy) of the glass equal those of the corresponding undercooled liquid at the same temperature (Mauro et al., 2009a). The addend K is the chemically invariant shift factor (Al-Mukadam et al., 2021a, 2021b, 2020; Di Genova et al., 2020b; Stabile et al., 2021; Yue et al., 2002). Because we used the DSC approach involving matching heating and cooling rates (see methodology), here T_f corresponds to T_{onset} (Fig. 1) (Al-Mukadam et al., 2020; Di Genova et al., 2020b). As such, Eq. 5 can be written as (Eq. 6) :

$$log_{10}\eta(T_{onset}) = K_{onset} - log_{10}(q_h) \qquad (6)$$

where $K_{onset} = 11.20 \pm 0.15$ (Di Genova et al., 2020b; Stabile et al., 2021). Therefore, when q_h = 10 K min^{-1} (0.17 K s^{-1}), one has $\eta(T_{onset}) \approx 10^{12}$ Pa s and thus $T_{onset} \equiv T_g$, which can be directly inserted into the MYEGA equation to obtain a full viscosity parameterization without the need of data fitting ($\log_{10}\eta_\infty = -2.93 \pm 0.3$ and m is obtained spectroscopically). In such cases, the agreement with experimental viscosity data obtained by micropenetration viscometry or additional DSC measurements performed at different q_h can be used to validate this approach. Additionally, several studies (Stabile et al., 2021 and references therein) demonstrated that with Eq. 5 one can also derive the melt viscosity at T_{peak} (Fig. 1) of the heat flow (Eq. 7):

$$log_{10}\eta\left(T_{peak}\right) = K_{peak} - log_{10}(q_h) \qquad (7)$$

where $K_{peak} = 9.84 \pm 0.20$ (Di Genova et al., 2020b; Stabile et al., 2021).

The hydrous samples synthesized by the rapid-quench multi-anvil technique (Bondar et al., 2022) are too unstable and small to be characterized by conventional DSC or viscometry. Their viscosity can therefore be derived through rate-matching flash DSC measurements in the range $10^{9.2}$-$10^{6.4}$ Pa s, subsequently fitting the value of T_g in Eq. 1 using these data points ($\log_{10}\eta_\infty = -2.93 \pm 0.3$ and m is obtained spectroscopically).

2. Materials and methods

2.1. Peridotite glass synthesis

Anhydrous and hydrous glasses are identified by a nomenclature mirroring their chemical composition, namely: S_F_W_, where S and F respectively stand for the SiO_2 and FeO_{tot} molar contents of the base anhydrous glass and W for the H_2O molar content. This choice enables straightforward identification of samples with a similar anhydrous base composition, but different water contents. Anhydrous glasses were synthesized in containerless conditions at the CEMHTI laboratory in Orléans (France), using the aerodynamic levitation device coupled to laser heating (ADL) detailed elsewhere (Zandona et al., 2022). The device consists of two CO_2 lasers (wavelength: 10.6 µm; maximum power: 250 W) heating from above and below a sample weighing a few tens of milligrams and suspended in a copper nozzle by a gas jet (Ar or O_2).

For the syntheses, laboratory-grade SiO_2 (99.9%, Chempur), Al_2O_3 (99.999%, Strem Chemicals), MgO (99.5%, Strem Chemicals), FeO (99.9%, Aldrich), Fe_2O_3 (68.2-71.7 %Fe, Sigma-Aldrich) and $CaCO_3$ (99.95%, Strem Chemicals) were weighed in the right proportions, mixed thoroughly in an agate mortar with the addition of ethanol, dried, and compacted with a hydraulic press into cylindrical pellets of approximately 1 g. Small chunks of these pellets were then introduced into the ADL nozzle and melted by quickly ramping up the laser power until full liquefaction of the materials was achieved, at pyrometer readings (wavelength: 0.9 μm) in the range 1800 – 2100 ˚C depending on composition. After holding at the maximum temperature for ~5 s for homogenization, the melts were quenched into glasses by instantaneously shutting off the lasers, which typically yields cooling rates in the order of a few hundreds of kelvins per second. No signs of high-temperature volatilization (smoke or material deposition on the nozzle wall) were detected using this procedure. Samples were synthesized using FeO as raw material and Ar as a levitation gas. To explore the effect of different oxy-reduction conditions, two samples (S44F6+ and S44F12+) were obtained using Fe_2O_3 in the starting powder mixtures and pure O_2 as a levitation gas.

The set of four hydrous peridotite glasses was previously synthesized at confining pressure of 0.9 GPa using a 15-MN Kawai-type multi-anvil press equipped with a novel rapid-quench multi-anvil technique (Bondar et al., 2021, 2020). The detailed description and synthesis conditions of glasses S38F5W1, S40F5W6, S43F7W8 and S39F6W12 (referred to as I1075, I1045, I867 and I1111, respectively, in the previous study) are given in (Bondar et al., 2022).

2.2. Electron microprobe analyses

Major element compositions of glasses were determined using a JEOL JXA-8200 electron probe microanalyzer equipped with five wavelength-dispersive spectrometers at the Bayerisches Geoinstitut (BGI), University of Bayreuth (Germany). Samples were carbon-coated with a thickness of 12 nm before analysis. Oxygen was calculated by stoichiometry, and all the iron was assigned as ferrous iron. Glasses were analyzed with a defocused 10 μm beam using 15 kV accelerating voltage, 5 nA beam current, a peak counting time of 20 s and a background counting time of 10 s. Measured peak counts were corrected using the PRZ (Phi-Rho-Z) method

(Armstrong, 1991). Standards included wollastonite (Si, Ca), hematite (Fe), periclase (Mg), spinel (Al), albite (Na), orthoclase (K), manganese titanate (Ti, Mn), and chromium metal (Cr). Results of the analyses are reported in Tab. 1.

*Table 1. Chemical composition (mol%) of samples used and considered in this study. Uncertainties are reported in parenthesis for each value. References: *this study, [1](Bondar et al., 2022), [2](Bondar, 2023), [3](Dingwell et al., 2004). Water contents in H_2O-bearing glasses were determined by a combination of elastic recoil detection analysis and secondary ion mass spectrometry (Bondar, 2023).*

Sample	SiO_2	TiO_2	Al_2O_3	FeO_{tot}	MnO	MgO	CaO	Na_2O	K_2O	P_2O_5	Cr_2O_3	H_2O	$Fe^{3+}/Fe_{tot.}$	Ref.
S44F0	44.16 (0.15)	0.02 (0.02)	3.39 (0.04)	0.05 (0.02)	0.01 (0.01)	45.68 (0.17)	6.64 (0.12)	0.02 (0.02)	0.01 (0.01)	0.02 (0.02)	n.a.	b.d.l.[a]	-	*
S44F6+	43.67 (0.21)	0.01 (0.01)	3.37 (0.05)	6.19 (0.12)	0.01 (0.01)	40.05 (0.22)	6.63 (0.12)	0.03 (0.02)	0.02 (0.01)	b.d.l.	n.a.	b.d.l.[a]	0.54 (0.05)	*
S44F6	43.28 (0.20)	0.01 (0.01)	3.43 (0.06)	6.40 (0.11)	0.01 (0.01)	40.32 (0.17)	6.49 (0.10)	0.02 (0.02)	0.02 (0.01)	0.01 (0.01)	n.a.	b.d.l.[a]	0.38 (0.05)	*
S44F12+	43.11 (0.17)	0.02 (0.02)	3.36 (0.05)	12.10 (0.14)	0.01 (0.01)	34.65 (0.20)	6.70 (0.10)	b.d.l.	0.02 (0.01)	0.02 (0.02)	n.a.	b.d.l.[a]	0.50 (0.05)	*
S44F12	43.21 (0.25)	0.02 (0.02)	3.29 (0.05)	12.29 (0.19)	0.02 (0.02)	34.57 (0.23)	6.55 (0.11)	0.02 (0.02)	0.02 (0.01)	0.01 (0.01)	n.a.	b.d.l.[a]	0.31 (0.04)	*
S40F6	40.41 (0.21)	0.01 (0.01)	2.07 (0.04)	6.41 (0.08)	0.01 (0.01)	47.78 (0.23)	3.27 (0.08)	0.02 (0.02)	0.01 (0.01)	0.01 (0.01)	n.a.	b.d.l.[a]	0.32 (0.04)	*
S45F7	45.44 (0.18)	0.01 (0.01)	2.15 (0.05)	6.67 (0.11)	0.01 (0.01)	42.67 (0.19)	3.00 (0.08)	0.01 (0.01)	0.02 (0.01)	0.01 (0.01)	n.a.	b.d.l.[a]	0.34 (0.04)	*
S34F0	33.71 (0.17)	0.01 (0.01)	2.03 (0.04)	0.05 (0.02)	b.d.l.	48.98 (0.16)	15.19 (0.16)	0.01 (0.01)	b.d.l.	0.01 (0.01)	n.a.	b.d.l.[a]	-	*
S38F5W1	37.72 (0.14)	0.13 (0.02)	1.59 (0.03)	5.37 (0.06)	0.11 (0.02)	51.44 (0.13)	2.73 (0.06)	0.17 (0.02)	0.02 (0.01)	n.a.	0.07 (0.01)	0.65 (0.06)	n.a.	1, 2, *
S40F5W6	37.34 (0.21)	0.13 (0.02)	1.84 (0.06)	4.32 (0.09)	0.09 (0.01)	47.91 (0.22)	2.58 (0.07)	0.18 (0.03)	0.03 (0.01)	n.a.	0.07 (0.01)	5.51 (0.52)	n.a.	1, 2, *
S43F7W8	39.10 (0.20)	0.20 (0.03)	2.28 (0.04)	6.13 (0.08)	0.12 (0.02)	39.87 (0.20)	3.82 (0.06)	0.23 (0.02)	0.03 (0.01)	n.a.	0.08 (0.01)	8.13 (0.77)	n.a.	1, 2, *
S39F6W12	33.75 (0.19)	0.08 (0.02)	1.39 (0.04)	4.86 (0.07)	0.06 (0.02)	46.38 (0.14)	1.68 (0.08)	0.12 (0.02)	0.01 (0.01)	n.a.	0.06 (0.01)	11.62 (1.10)	n.a.	1, 2, *
S42F7	41.54 (0.63)	0.12 (0.02)	2.60 (0.04)	6.53 (0.23)	n.a.	42.68 (0.67)	6.18 (0.16)	0.28 (0.02)	n.a.	n.a.	0.13 (0.02)	n.a.	n.a.	3

[a] no signal was detected in the near-infrared region around 3530 cm^{-1}, which corresponds to the asymmetrical broad band due to the fundamental O-H stretching vibrations in OH^- groups and H_2O molecules. It indicates that the glasses produced by ADL are essentially dry.

2.3. Mössbauer analyses

Glass pieces of roughly 2 mm diameter were embedded in epoxy that was cut into disks with thicknesses between 400 and 500 µm, which is close to the optimum thickness for these compositions. Mössbauer spectra were recorded at room temperature (293 K) in transmission mode on a constant acceleration Mössbauer spectrometer with a nominal 370 MBq ^{57}Co high specific activity (point) source in a 12 μm thick Rh matrix. The velocity scale was calibrated relative to 25 μm thick α-Fe foil and spectra were collected over the range ± 5 mm s^{-1} for 1 to 3 days each. Spectra were fitted with the full transmission integral using MossA software (Prescher et al., 2012). Values of Fe^{3+}/Fe_{tot} were calculated from relative areas and are listed in Tab. 1.

2.4. Raman spectroscopy

The as-prepared peridotite glasses were characterized by Raman spectroscopy on optically polished surfaces using a Renishaw Invia Reflex Raman spectrometer equipped with a 514 nm green laser (50 mW nominal power, operated at 10%) and a 1800 mm^{-1} grating. Spectra were acquired with a 100x objective in the ranges 200–1500 cm^{-1} and 2700–4000 cm^{-1}, with 30 s acquisition time and 2 accumulations. The samples subjected to DSC and micropenetration were also characterized before and after the measurements using a confocal Raman imaging microscope (alpha300R, WITec GmbH) at the Institute of Non-Metallic Materials, Clausthal University of Technology (Germany). The Raman microscope is equipped with a 100x objective, a 532 nm diode green laser and a CCD detector. The integration time employed with the alpha300R microscope was 7 s (3 accumulations, 13 mW laser power). Raman spectra were invariably collected on polished or cleanly broken surfaces, to exclude possible surface effects. Spectra were acquired in the range from 200 to 1300 cm^{-1}. The Raman spectrometer was calibrated using a silicon standard.

2.5. Calorimetry

We subjected ~20 ± 5 mg of glass to controlled heat treatments in a conventional differential scanning calorimeter at the Institute of Non-Metallic Materials, Clausthal University of Technology (CDSC, 404 C, Netzsch) using PtRh20 crucibles and under N_2 5.0 (≥99.999%

purity) atmosphere. Moreover, we used a few ng for flash calorimetry measurements (FDSC, Mettler Toledo Flash DSC 2+ equipped with a UFH 1 sensor), under constant gas flow (40 ml min^{-1}) of Ar 5.0. The CDSC was calibrated using melting temperatures and enthalpy of fusion of reference materials (pure metals: In, Sn, Bi, Zn, Al, Ag, and Au) up to 1337 K. The FDSC was calibrated using the melting temperature of aluminium (melting temperature 933.6 K) and indium (melting temperature 429.8 K).

We employed the matching rates methodology (Stabile et al., 2021) to measure the characteristic temperatures T_{onset} and T_{peak} (Fig. 1). For the CDSC, we first allowed sample relaxation by heating the starting material at 20 K min^{-1} from room temperature to the glass transition interval. Afterwards, the sample was cooled at a q_c of either 10 or 20 K min^{-1} down to 373 K and subsequently heated at $q_h \equiv q_c$ (i.e, matching rates). For the FDSC, we used the same procedure but at higher q_h (from 6,000 to 1,800,000 K min^{-1}, namely from 100 to 30,000 K s^{-1}) listed in Tab. 3. T_{onset} represents the onset of the glass transition interval: it corresponds to the intersection of two tangents, the first applied to the calorimetric trace pertaining to the glass and the second at the inflection point during the glass transition, this latter identified as zero point on the first derivative of the signal. It should be noted that T_{onset} can be more precisely identified using a recently described method (Mancini et al., 2021), which however requires a 4-fold repetition of the measurement (impractical for samples of small size and strong crystallization tendency) and a smoothing of the average curve. On the other hand, T_{peak}, which is identified as the minimum on the second derivative of the signal, represents the signal undershoot of the matching upscan in Figure 1 (Al-Mukadam et al., 2021b, 2020; Di Genova et al., 2020b).

Further details about the fast heating and cooling of the FDSC, especially the differences with respect to the CDSD, are described in previous studies and patents (Vanden Poel et al., 2012, 2011). In short, the FDSC chip sensor has four thermocouples in total, which guarantee high sensitivity and high temperature resolution. The temperature resolution is enhanced by a lower time constant of the sensor, which is ~0.2 ms in the FDSC, that is approximately ~10,000 times less than that of a CDSC instrument.

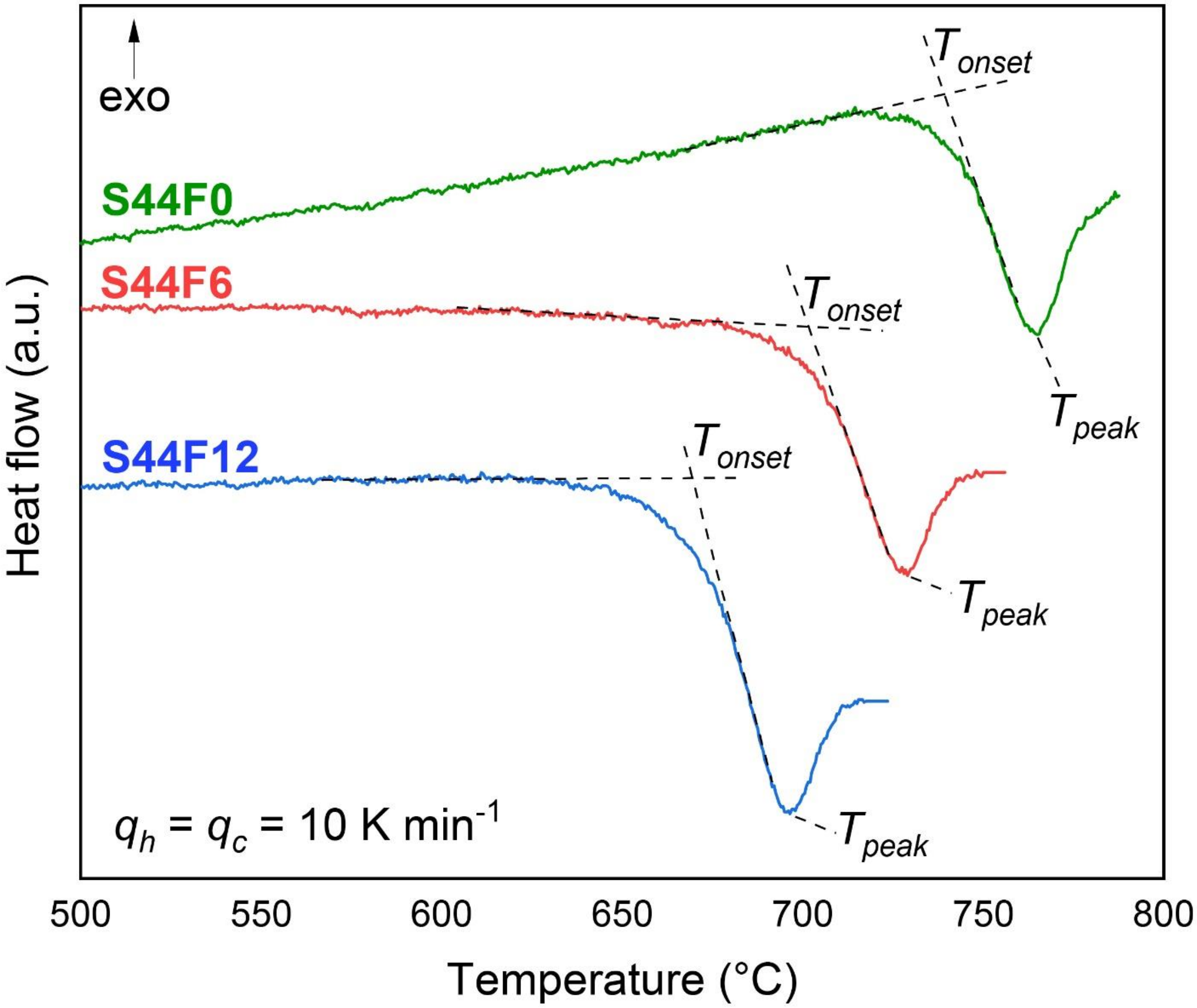

Figure 1. Measured heat flow using a conventional DSC as a function of temperature for samples S44F0, S44F6 and S44F12 at a heating rate of 10 K min^{-1}, following a cooling rate of 10 K min^{-1} through the glass transition interval. The characteristic glass transition temperatures (T_{onset} and T_{peak}) are shown in the figure. a.u. – arbitrary units.

2.6. Micropenetration viscometry

We subjected polished plane-parallel glass chips (2-2.5 mm thick) to micropenetration viscometry measurements. We used a vertical dilatometer (Bähr VIS 404) at the Institute of Non-Metallic Materials, Clausthal University of Technology. The setup consists of a SiO_2 rod pushing a sapphire sphere of radius $r = 0.75$ mm, under a constant Ar flow, using a force of 3.92 N (400 g load). The temperature was controlled with an S-type thermocouple (Pt-PtRh) placed at ~2 mm from the sample surface. The temperature error is estimated at ±5 K considering the accuracy of the S-type thermocouple and its distance from the sample (Behrens et al., 2018). We followed standard procedures (Di Genova et al., 2014a) to achieve thermal equilibration of the sample at the target measuring temperature: a heating rate of 10 K min^{-1} was used up to a temperature 100 K lower than the target temperature, which was then approached with a slower heating rate of 5 K min^{-1}. After reaching the final dwell temperature, the samples were allowed to relax before the load was applied. The indentation depth of the sapphire sphere into the sample was measured as a function of time using a linear variable displacement transducer and viscosity was determined according to the literature (Douglas et al., 1965). Viscosity measurements of the standard glass DGG-1 were used to calibrate the vertical dilatometer. The certified viscosity data (Meerlender, 1974) were reproduced with a standard deviation of ± 0.1 in log units.

2.7. Brillouin spectroscopy

Prior to Brillouin scattering measurements, samples were double-polished to a thickness of approximately 50 µm. The measurements were conducted using the system installed at BGI (Trots et al., 2013), which includes a Coherent Verdi V2 solid-state Nd:YVO_4 laser with a 532 nm single wavelength output and a six-pass Sandercock-type tandem Fabry-Perot interferometer equipped with a Hamamatsu C11202-050 single-pixel photon-counting module. Focusing-collecting optics with 100 mm focal lengths were employed to focus the laser beam on the sample position and to collect the scattered inelastic signal. A laser power of 0.03 W was used in all measurements. The measurements were performed in a forward platelet symmetric geometry with an angle of 80° between the incident and scattered beams. This geometry allows the refractive index of the sample to be neglected when calculating sound velocities from the frequency shifts of inelastically scattered photons (Sinogeikin et al., 2006; Whitfield et al., 1976). Measurements were repeated 4 to 8 times at different azimuthal angles to account for possible platelet tilt or polishing imperfection. As the acoustic wave velocities in isotropic solids are independent on sample orientation, results at different angles were averaged. Experimentally determined Brillouin frequency shifts $\Delta\omega$ were converted to longitudinal v_p and shear v_s sound velocities according to the equation (Eq. 8):

$$v = \frac{\Delta\omega\lambda}{2sin(\theta/2)} \qquad (8)$$

where λ is the laser wavelength and θ is the angle between the incident and scattered beams (Sinogeikin et al., 2006; Whitfield et al., 1976).

3. Results

3.1 Overall characterization and vibrational spectroscopies

Table 1 lists the chemical composition of the glasses (mol%) considered in this study, determined by electron microprobe analysis; Fe^{3+}/Fe_{tot} ratios were obtained by Mössbauer spectroscopy. The amorphous nature of these hydrous and anhydrous peridotite glasses was confirmed by Raman spectroscopy (Fig. 2): the obtained Raman spectra matched well with those reported by previous authors for similar compositions (Bondar et al., 2022; Cooney and Sharma, 1990; Durben et al., 1993; Williams et al., 1989). In particular, we observed the general absence of intense vibrational features at low wavenumber (<600 cm^{-1}) and the invariable occurrence of a broad vibrational envelope in the range 800–1100 cm^{-1}, following the substantial structural depolymerization of these glasses as inferred by the theoretical number of non-bridging oxygens per atom of a tetrahedrally coordinated cation NBO/T ≈ 2.9 (Bondar et al., 2022). The substitution of up to 12 mol% MgO by FeO (as in sample S44F12 compared to S44F0) and the different Fe^{3+}/Fe_{tot} ratios obtained by O_2 or Ar melting (as in S44F12 and S44F12+) did not seem to have appreciable effects on the Raman spectra. Only S34F0 markedly differed from the other melt-quenched glasses, most likely due to its much lower SiO_2 content: its spectrum is very similar to that of pure forsterite glass (Williams et al., 1989). The observation of vibrational features at ~3600 cm^{-1} in hyperquenched high-pressure peridotite glasses confirmed the successful incorporation of H_2O in their structure. As noticed previously (Bondar et al., 2022), the high-wavenumber envelope of these hydrous glasses was shifted to higher wavenumbers as compared to their anhydrous counterparts, which could suggest partial water-driven repolymerization (Xue and Kanzaki, 2004) or a different Fe^{3+}/Fe_{tot} ratio (Di Genova et al., 2016b).

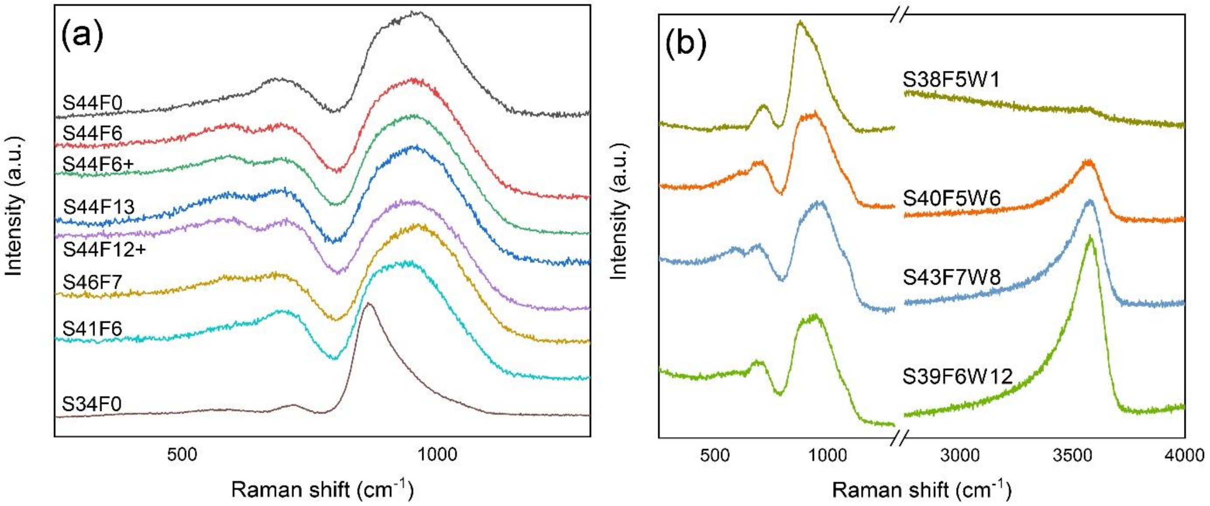

Figure 2. Raman spectra of peridotite glasses synthesized within this work. (a) Anhydrous peridotite glasses synthesized by ADL, dominated by an intense high-wavenumber envelope manifesting their extreme structural depolymerization. (b) Hydrous peridotite glasses synthesized using a novel rapid-quench multi-anvil technique, in which the incorporation of water is demonstrated by the appearance of intense Raman features at ~3500 cm^{-1}.

Table 2. Measured acoustic wave velocities (v_s and v_p), calculated elastic moduli ratio (K/G, Eq. 4), and melt fragility (m, Eq. 3) for all samples synthesized within this work. Numers in parentheses provide the uncertainty of the last digit(s).

Sample	v_s (m s^{-1})	v_p (m s^{-1})	*K/G*	*m*
S44F0	3826 (1)	6953 (5)	1.97 (1)	54.7 (1)
S44F6+	3757 (3)	6850 (5)	1.99 (1)	55.6 (2)
S44F6	3718 (3)	6825 (3)	2.04 (1)	57.6 (2)
S44F12+	3627 (3)	6695 (3)	2.07 (1)	59.2 (2)
S44F12	3636 (3)	6697 (3)	2.06 (1)	58.6 (2)
S41F6	3755 (7)	6917 (4)	2.06 (1)	58.6 (2)
S46F7	3736 (4)	6822 (1)	2.00 (1)	55.9 (2)
S34F0	3819 (9)	7016 (9)	2.04 (2)	57.8 (5)
S38F5W1	3774 (3)	6965 (4)	2.07 (1)	59.1 (2)
S40F5W6	3835 (5)	6989 (5)	1.99 (1)	55.5 (3)
S43F7W8	3768 (9)	6815 (16)	1.94 (2)	53.3 (6)
S39F6W12	3830 (4)	6899 (5)	1.91 (1)	52.1 (2)

The measured shear v_s and longitudinal v_p acoustic wave velocities, the calculated elastic moduli ratio *K/G* and fragility index *m* are reported in Tab. 2. The iron content (FeO$_{tot.}$ in mol%) appeared to be the main compositional parameter controlling the acoustic wave velocities in the measured anhydrous samples (Fig. 3a). The iron-free S44F0 and S34F0 glasses exhibited the highest recorded velocities, with v_s 3826(1) and 3819(9) m s^{-1} and v_p 6953(5) and 7016(9) m s^{-1}, respectively. In contrast, the most Fe-rich samples S44F12 and S44F12+ showed the lowest v_s (respectively 3636(3) and 3627(3) m s^{-1}) and v_p values (respectively 6697(3) and 6695(3) m s^{-1}). Samples with an intermediate iron content plot in between.

The calculated *K/G* values (Eq. 4) exhibited a similar dependence on the FeO_{tot} content, superimposed on the influence of the overall SiO_2 content of the glasses, as expected from previous results (Cassetta et al., 2021). Within the S44F series (Fig. 3b), *K/G* ratios increased from 1.97(1) (S44F0) to 2.07(1) (S44F12+ and S44F12), with S44F6 and S44F6+ plotting at intermediate values (2.04(1) and 1.99(1), respectively). At similar FeO_{tot} contents (i.e., S44F0 and S34F0), SiO_2-richer samples exhibited instead a substantially lower *K/G*.

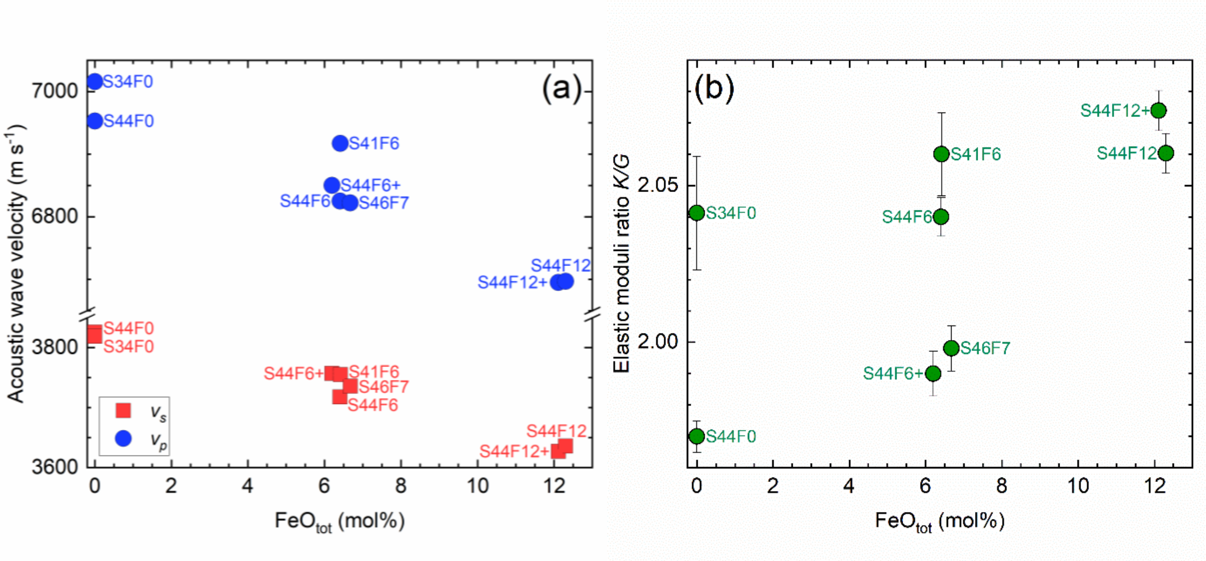

Figure 3. Results of BLS measurements performed on anhydrous peridotite glasses, plotted as a function of their $FeO_{tot.}$ content (mol%). (a) Acoustic wave velocities generally decrease as FeO_{tot} increases, while (b) K/G ratios exhibit the opposite behaviour, superposed by a lesser dependence on the SiO_2 content of the glasses. Whenever absent, error bars are smaller than the depicted symbols.

For the hydrous samples ($FeO_{tot.}$ = 5.2 ± 1 mol%), acoustic wave velocities v_s and v_p did not exhibit a clear dependence on water content (Fig. 4), which ranged between 0.65 (S38F5W1) and 11.62 mol% (S39F6W12). Nevertheless, the *K/G* ratio decreased proportionally to the degree of hydration, to the point that glass S39F6W12 showed the lowest recorded value in this study (1.91(1)) despite the very low overall SiO_2 content (~34 mol%, i.e., ~39 mol% of its anhydrous base composition). Although the measured K/G ratios locate slightly outside the range investigated previously (Cassetta et al., 2021), we converted *K/G* ratios into fragility *m* using Eq. 3: S39F6W12 showed the lowest *m* (52.1(2)), whereas S44F12+ (anhydrous, highest $FeO_{tot.}$) exhibited the highest value (59.2(2)).

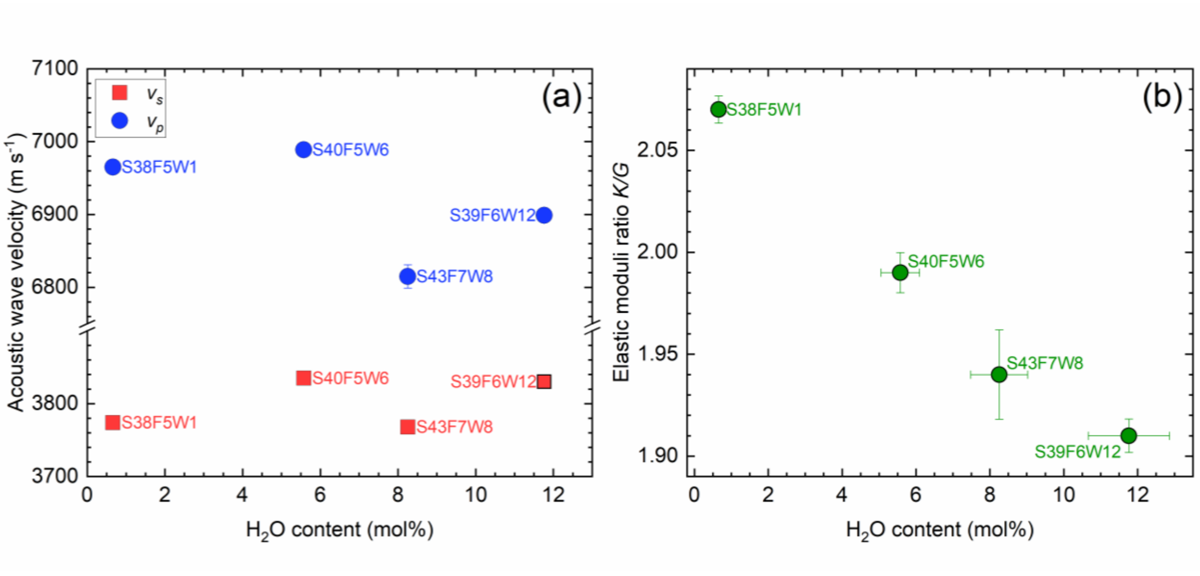

Figure 4. Results of BLS measurements performed on hydrous peridotite glasses, plotted as a function of their H_2O content. (a) Acoustic wave velocities do not show an appreciable trend, but (b) K/G ratios clearly decrease proportionally to the hydration degree of the glasses. Whenever absent, error bars are smaller than the depicted symbols.

3.2 (Flash) calorimetry

Table 3 lists the measured characteristic temperatures T_{onset} and T_{peak} as a function of the heating rate: anhydrous samples could be characterized by CDSC (q_h = 10 and 20 K min^{-1}), while the low available amounts and high instability of hydrous glasses made them suitable only for FDSC (q_h = 100 and 30,000 K s^{-1}). In agreement with the literature (Di Genova et al., 2014b), the values of T_{onset} and T_{peak} increased with increasing q_h for both anhydrous and hydrous samples.

As observed for the sound velocities (Fig. 3), FeO_{tot} stood out as the major compositional parameter controlling T_{onset} and T_{peak} in anhydrous samples, as they both decreased with increasing iron content (Fig. 5). At q_h = 10 K min^{-1}, the highest T_{onset} and T_{peak} were obtained from S34F0 sample (1029 ± 3 and 1051 ± 1 K, respectively), whereas S44F12 showed the lowest T_{onset} and T_{peak} (942 ± 3 and 969 ± 1 K, respectively). In samples with the same molar content of FeO_{tot} (e.g., S34F0 and S44F0), SiO_2 depletion seemed to lead to an increase in T_{onset} and T_{peak}. In line with the literature (e.g., Bouhifd et al., 2004; Chevrel et al., 2013; Cukierman and Uhlmann, 1974; Di Genova et al., 2017c), we measured (Tab. 3) a systematic effect of iron oxidation (Tab. 1) on the DSC results: samples with a higher Fe^{3+}/Fe_{tot} (S44F6+ and S44F12+) exhibited slightly higher T_{onset} and T_{peak} than the reduced counterparts (S44F6 and S44F12).

Table 3. Results of calorimetric measurements performed on peridotite glasses, from this work and a literature reference (Dingwell et al., 2004). Viscosities associated with T_{onset} and T_{peak} for all samples were calculated using Eq. 3 and shift factors (K_{onset} and K_{peak}) used in this study. Temperature uncertainty (±1 K for T_{peak}, ±3 K for T_{onset}) was estimated based on repeated measurements (only one for each sample and heating rate is reported here for brevity) and calibration. Uncertainties for viscosity were estimated in a previous work (Di Genova et al., 2020b), *i.e.* ±0.15 *for* T_{onset} *and* ±0.20 *for* T_{peak}. *References: *this study, and* [1] *(Dingwell et al., 2004).*

Method	Sample	q (K min^{-1})	q (K s^{-1})	T_{onset} (K)	$\log_{10}\eta$ (η in Pa s)	T_{peak} (K)	$\log_{10}\eta$ (η in Pa s)	Ref.
CDSC	S44F0	10	0.17	1,014	11.98	1,038	10.62	*
		20	0.33	1,019	11.68	1,046	10.32	
	S44F6+	10	0.17	976	11.98	1,003	10.62	*
		20	0.33	983	11.68	1,010	10.32	
	S44F6	10	0.17	974	11.98	1,002	10.62	*
		20	0.33	982	11.68	1,009	10.32	
	S44F12+	10	0.17	947	11.98	975	10.62	*
		20	0.33	956	11.68	984	10.32	
	S44F12	10	0.17	942	11.98	969	10.62	*
		20	0.33	950	11.68	977	10.32	
	S41F6	10	0.17	990	11.98	1,011	10.62	*
	S46F7	10	0.17	985	11.98	1,010	10.62	*
	S34F0	10	0.17	1,029	11.98	1,050	10.62	*
	S42F7	5	0.08			1,006	10.92	1
		8	0.13			1,013	10.72	
		10	0.17			1,013	10.62	
		15	0.25			1,017	10.44	
		20	0.33			1,018	10.32	
FDSC	S38F5W1	6,000	100	1,025	9.20	1,066	7.84	*
		12,000	200	1,036	8.90	1,072	7.54	
		18,000	300	1,041	8.72	1,075	7.36	
		30,000	500	1,045	8.50	1,080	7.14	
		60,000	1,000	1,055	8.20	1,090	6.84	
		180,000	3,000	1,069	7.72	1,109	6.36	
		300,000	5,000	1,074	7.50			
		420,000	7,000	1,077	7.35			
		600,000	10,000	1,084	7.20			
		1,200,000	20,000	1,095	6.90			
		1,800,000	30,000	1,098	6.72			
	S40F5W6	60,000	1,000	938	8.20	1,007	6.84	*
	S43F7W8	60,000	1,000	896	8.20	960	6.84	*
	S39F6W12	60,000	1,000	879	8.20			*

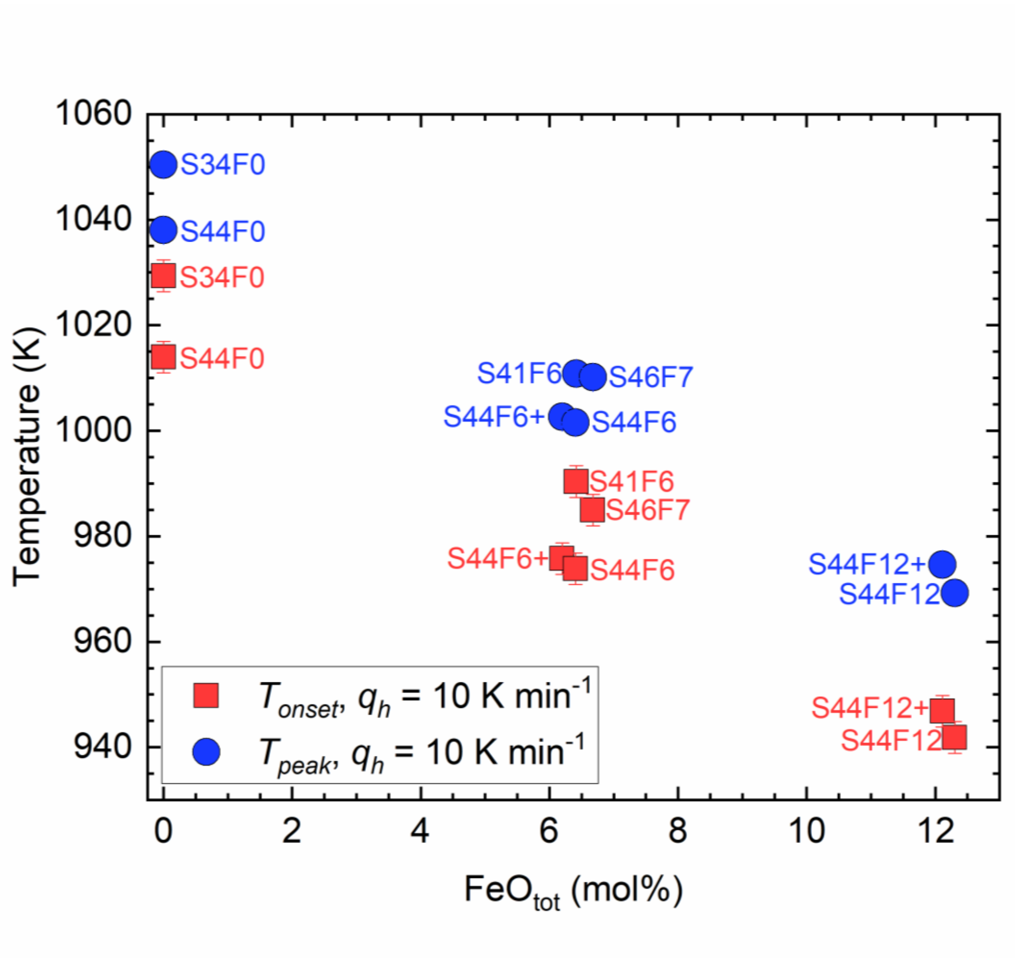

Figure 5. Characteristic temperatures T_{onset} and T_{peak} of anhydrous peridotite glasses obtained from conventional DSC measurements performed at 10 K min^{-1}, plotted as a function of their FeO_{tot} content. T_{onset} and T_{peak} exhibit an overall reduction as the FeO_{tot} content of the glasses increases. Whenever absent, error bars are smaller than the depicted symbols.

Due to the instability of hydrous peridotite glasses, we used the most H_2O-poor sample (S38F5W1) to successfully test the reproducibility of our FDSC approach, performing measurements of T_{onset} and T_{peak} at the standard rate q_h = 1000 K s^{-1} before and after any other calorimetric run at a different heating rate (Fig. 6a, Fig. S1 and Tab. 3). Comparison of the values obtained at q_h = 1000 K s^{-1} revealed any sample modification through a shift in the values of T_{onset} and T_{peak}; when such deviations were observed, Raman spectra were acquired to document that the sample changed during the measurement (i.e., crystallization and/or degassing). We indeed demonstrated in several recent works that Raman spectroscopy can reveal the precipitation of nanosized Fe-Ti-oxides (as expected during calorimetric measurements of magmatic melts at deep undercooling, where transition metals are poorly soluble and homogeneous crystal nucleation prevails over crystal growth), with sensitivity extending even to the early stages of amorphous phase separation anticipating the occurrence of actual crystals (Di Genova et al., 2020b, 2020a, 2017a, 2017b; Scarani et al., 2022; Zandona et al., 2022, 2021, 2019). Using this approach, we concluded that sample S38F5W1 may be reliably measured for q_h ranging between 100 and 30000 K s^{-1} (see the expected linear dependence on q_h in Figure 6); we obtained T_{onset} = 1055 ± 3 K and T_{peak} = 1090 ± 1 K at q_h = 1000 K s^{-1}. For $q_h \geq$ 5,000 K s^{-1} we limited the matching upscans to temperatures $\leq T_{peak}$, as the exposure of the melt to higher temperatures induced partial crystallization (Di Genova et al., 2020b; Scarani et al., 2022), inferred from the opacification of the glass and the appearance of the sharp characteristic features (e.g., at ~670 cm^{-1}) of Fe-Ti-oxide crystals in its Raman spectrum (Di Genova et al., 2020a, 2020b, 2017b).

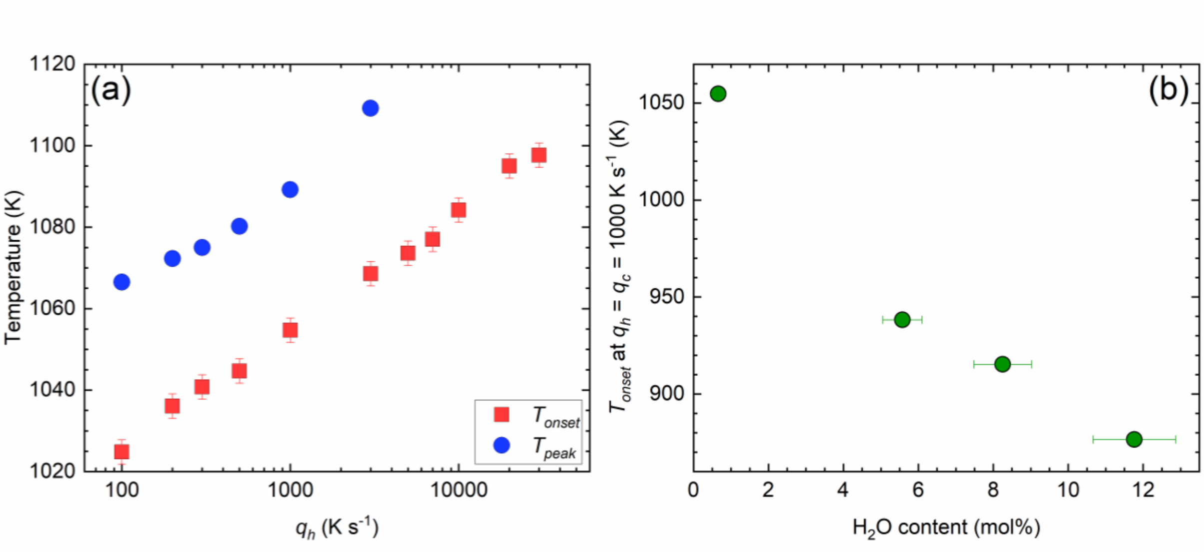

Figure 6. Results of flash DSC measurements performed on hydrous peridotite glasses. (a) T_{onset} and T_{peak} obtained from sample S38F5W1, plotted as a function of the applied heating rate q_h. The linear trend confirms the absence of sample modification (e.g. crystallization and degassing)

during the measurements. (b) T_{onset} values obtained at 1000 K min^{-1} from all hydrous peridotite glasses, plotted as a function of the water molar content: the higher the water content, the lower T_{onset}. Whenever absent, error bars are smaller than the depicted symbols.

For samples with increasing water content (from 5.51 to 11.62 mol%), however, we collected T_{onset} and T_{peak} only at q_h = 1000 K s^{-1} (Fig. S2 and Tab. 3), since slower rates resulted in a low DSC signal and faster ones triggered crystallization and/or degassing due to the high-temperature exposure above T_f. No T_{peak} value could be acquired from sample S39F6W12, whose very high water content (11.62 mol%) led to instability that forced us to restrict the matching upscan to T_{onset}, thereby avoiding fast crystallization and/or degassing at higher temperatures.

The T_{onset} at q_h = 1000 K s^{-1} significantly decreased with increasing water content (Fig. 6b): we measured 1055, 938, 896 and 879 ± 3 K for samples S38F5W1, S40F5W6, S43F7W8 and S39F6W12, respectively.

3.3 Micropenetration viscometry

Table 4. Results of micropenetration viscometry measurements performed on some anhydrous peridotite glasses. Uncertainty is ± 0.1 in log unit based on calibration using DGG-1 standard glass (Meerlender, 1974).

Sample	Temperature (K)	$\log_{10} \eta$ (η in Pa s)
S44F0	1024	11.20
	1039	10.35
	1030	10.85
S44F6+	986	11.36
S44F6	984	11.36
	1001	10.50
S44F12+	957	11.40
	975	10.52
S44F12	952	11.52
	969	10.41

Table 4 lists the results of micropenetration viscometry that are plotted in Figure 7 as a function of the temperature. We explored the effect of temperature, iron content, and iron oxidation state on the melt viscosity using samples of the series S44F, characterized by the same SiO_2 content (~44 mol%) but different $FeO_{tot.}$ and Fe^{3+}/Fe_{tot}. As expected, the viscosity decreased with increasing temperature for all samples. An increasing $FeO_{tot.}$ (from 0 to 12 mol%) led to a significant viscosity reduction: the iron-free sample (S44F0) had the highest recorded viscosity ($10^{10.35}$ Pa s at 1039 K), while the sample with the highest $FeO_{tot.}$ (S44F12) exhibited a similar viscosity ($10^{10.41}$ Pa s) at a far lower temperature (969 K). Finally, we observed a minor effect of the iron oxidation state, namely reduced samples (S44F6 and S44F12) were systematically less viscous than oxidized samples (S44F6+ and S44F12+). For instance, S44F12 showed a viscosity of $10^{10.41}$ Pa s at 969 K ($Fe^{3+}/Fe_{tot} = 0.31$), whereas S44F12+ ($Fe^{3+}/Fe_{tot} = 0.50$) exhibited a slightly higher viscosity ($10^{10.52}$ Pa s) at a lower temperature (975 K).

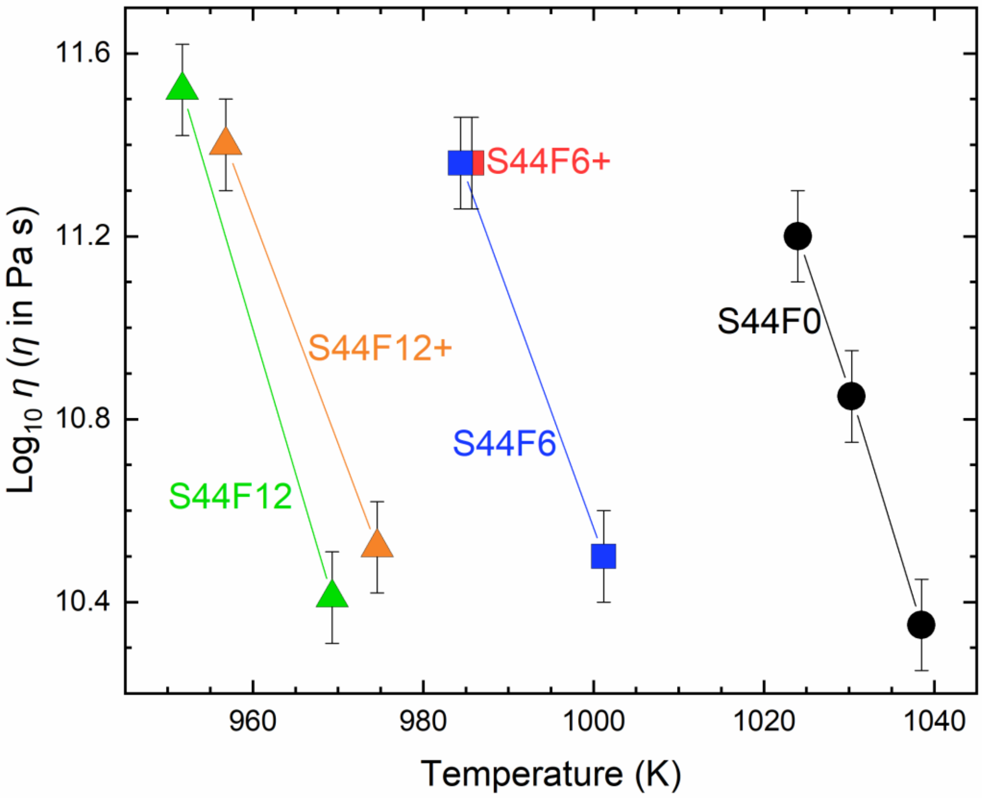

Figure 7. Results of micropenetration viscometry measurements performed on anhydrous peridotite glasses with different FeO$_{tot}$ content and Fe^{3+}/Fe$_{tot}$ ratio. A higher FeO$_{tot}$ content leads to lower viscosity values; more oxidized samples exhibit slightly higher viscosity than their reduced counterparts.

4. Discussion

4.1. Evaluation and comparison between existing viscosity models

We used measured (Tab. 4) and DSC-derived (Tab. 3) viscosity data obtained from our twelve anhydrous and hydrous peridotite glasses to test the performance of existing viscosity models. We calculated the melt viscosity of our anhydrous and hydrous samples using the measured chemical composition (Tab. 1). The Hui and Zhang (2007) model (HZ) is based on the empirical equation (Eq. 9):

$$\log_{10}\eta = A + \frac{B}{T} + \exp\left(C + \frac{D}{T}\right) \qquad \text{(Eq. 9)}$$

where T is the temperature and the A, B, C and D parameters are computed based on the melt composition. The Giordano–Russell–Dingwell model (GRD, Giordano et al., 2008) similarly employs composition to estimate B and C parameters of the VFTH equation (Eq. 10):

$$\log_{10}\eta = A + \frac{B}{T-C} \qquad \text{(Eq. 10)}$$

in which the viscosity at infinite temperature (A) is assumed constant ($10^{-4.55}$ Pa s) and iron is treated as a single species (e.g., $FeO_{tot.}$). The Langhammer–Di Genova–Steinle-Neumann model (LDS, Langhammer et al., 2022) is based on artificial neural networks trained on the largest viscosity database available for volcanic melts and also takes into account iron oxidation state; a web application is available online at https://domlang-visc-calc-final-script-a1hbsg.streamlitapp.com/

Figure 8a shows the comparison between our anhydrous micropenetration viscosity data and model predictions (10 observations). Our measurements are severely underestimated or overestimated by two of the selected models, respectively GRD and HZ. Conversely, the LDS model predicts well the data except for those collected from S44F12, the sample with the highest iron content and a comparatively low Fe^{3+}/Fe_{tot} ratio. For a general evaluation of the quality of the model predictions, we employed the root-mean-square error (RMSE) method and found that the models by GRD and HZ achieve RMSE of 2.75 and 4.32 respectively, whereas LDS has a RMSE of 1.25.

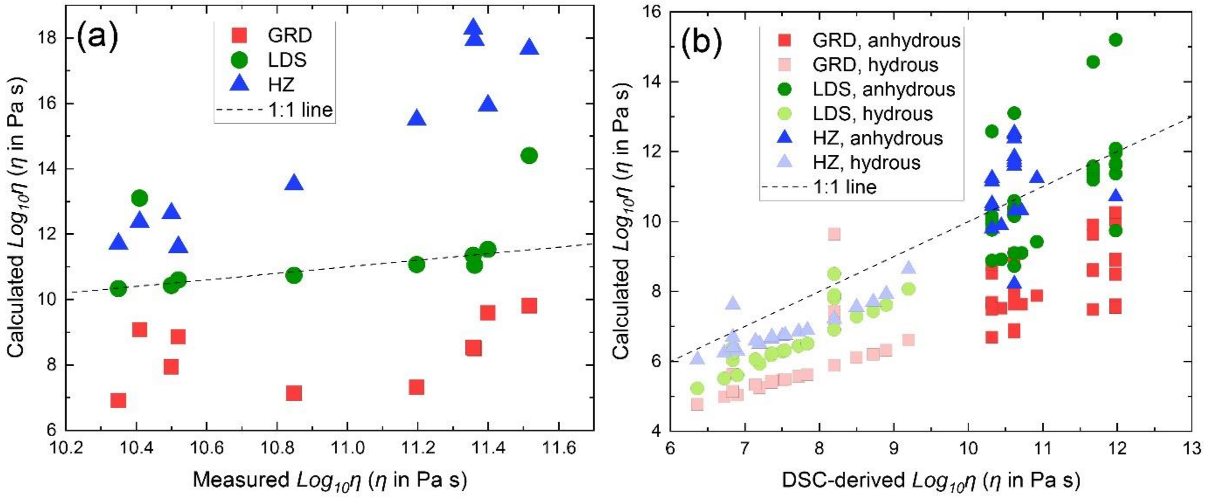

Figure 8. Comparison between viscosity data determined within this work and numerical model predictions. (a) Viscosity measured by micropenetration on anhydrous peridotite melts and the respective prediction using viscosity models from literature; (b) viscosity data derived from (flash) DSC measurements and literature data (Dingwell et al., 2004) on anhydrous and hydrous peridotite melts and the respective prediction using viscosity models. Considered models: GRD (Giordano et al., 2008), LDS (Langhammer et al., 2022) and HZ (Hui and Zhang, 2007). Error bars on measured data have been omitted for clarity.

Figure 8b similarly illustrates the comparison between anhydrous and hydrous DSC-derived viscosity data (77 data points, of which 53 are reported in Tab. 3 while the rest corresponds to repetitions of FDSC measurements performed to ensure reproducibility, using the same heating rate and the same sample) and the predictions of the models. Our measurements are mainly underestimated by all models with the one by LDS performing best. The HZ model performs well overall, but predicts unrealistically high viscosities of ~10^{20} Pa s for all T_{onset} at 10 and 20 K min^{-1} and $10^{34.74}$, $10^{18.75}$ and $10^{268.15}$ Pa s for the hydrous samples characterized by the highest water contents (5.51, 8.13 and 11.62 mol%, respectively). The predictions resulted in overall RMSE values of 1.21, 2.43 and 30.02 for LDS, GRD and HZ models, respectively.

4.2. Development of a viscosity model for peridotite melts

The experimental data gathered within this work enable a new tailored parameterization of the viscosity of peridotite melts as a function of temperature and water content. Figure 9 shows the modelled anhydrous viscosity (lines) for the S44F series using the MYEGA formulation (Eq. 1) the CDSC-derived T_g (i.e., T_{onset} at q_h = 10 K min^{-1} in Tab. 3) and the BLS-derived fragility index m (Eq. 3 and Tab. 2). For comparison, we also plot viscosity data points measured within this work (S44F series) and in the literature for S42F7 (Dingwell et al., 2004). Inspection of Figure 9 reveals that all experimental viscosity data points obtained by CDSC, micropenetration viscometry, and high-temperature concentric-cylinder viscometry are accurately predicted by our model, from T_g ($\eta = 10^{12}$ Pa s) down to $\eta \approx 10^{-1}$ Pa s (~1850 K). This remarkable result confirms that combining DSC and BLS (Cassetta et al., 2021) allows the reliable estimation of T_g and m and, thereby, the prediction and modelling of melt viscosity without the strict need for viscosity measurements; as evident, this approach can be reliably extended even to the exotic, highly depolymerized peridotite melts investigated in this study. Moreover, $K_{onset} = 11.20 \pm 0.15$ and $K_{peak} = 9.84 \pm 0.20$ are demonstrated to be chemically invariant for geological melts (Di Genova et al., 2020b; Stabile et al., 2021). Overall, our modelling shows that the combined effect of changing iron content and oxidation state (Fe^{3+}/Fe_{tot}) has a significant effect on melt viscosity, with the largest effect at around T_g ($\eta = 10^{12}$ Pa s). For instance, at 1014 K the viscosity decreases by more than three orders of magnitude from ~10^{12} Pa s for the iron-free sample (S44F0) to ~$10^{8.33}$ Pa s for the reduced sample with the highest $FeO_{tot.}$ (S44F12).

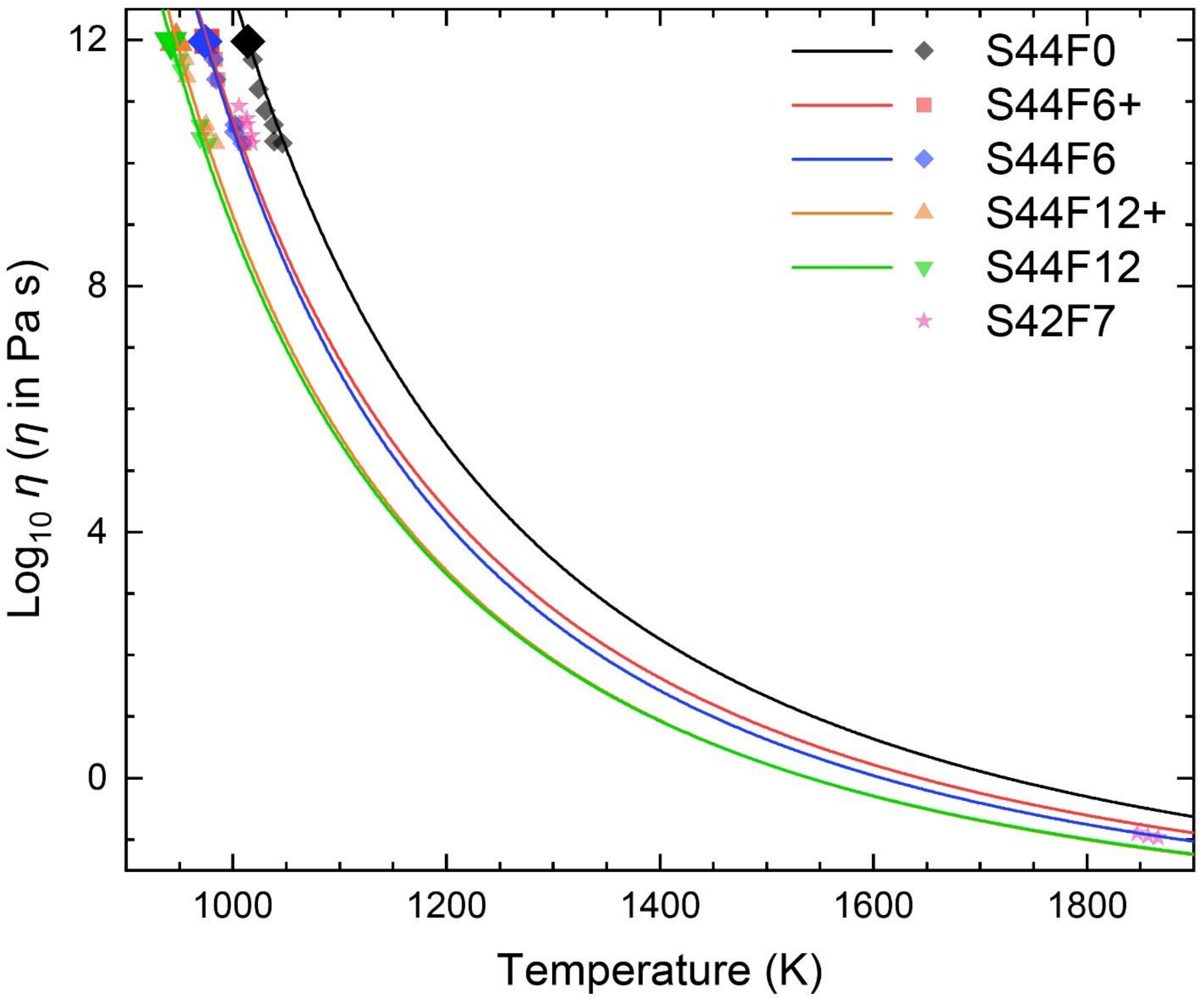

Figure 9. MYEGA parameterization (Eq. 1) of the viscosity of anhydrous peridotite melts, based on DSC-derived T_g and BLS-computed fragility values m. A higher FeO_{tot} content perceivably lowers the viscosity of peridotite melts. Experimental viscosity data from this work and literature (pink stars, from Dingwell et al., 2004) are reported for comparison. Error bars are smaller than the depicted symbols.

Modelling the viscosity of hydrous melts requires the knowledge of T_g as a function of water content. Direct T_g determination of hydrous samples could not be performed here because their size (in the order of ng) was suitable only for FDSC and not for CDSC measurements. For this reason, we obtained the values of T_g (η = 10^{12} Pa s) of our hydrous samples by fitting the MYEGA equation (Eq. 1) to the FDSC-derived viscosity datapoints (η in the range 10^9 – 10^6 Pa s, as in Tab. 3), and by fixing fragility *m* to the value derived by BLS (Tab. 2). Figure 10 shows how the obtained T_g values decrease as expected with increasing water content: we found that T_g decreases by ~11% (from 976 to 865 K) from 0.7 to 5.5 mol% of water, while the reduction is by ~14% for H_2O = 8.1 mol% (T_g = 841 K) and ~18% for H_2O = 11.6 mol% (T_g = 804 K). Our findings are in line with T_g measurements of depolymerized melts such as foidite (NBO/T = 1.5) and tephrite (NBO/T = 0.9) from the literature (Bouhifd et al., 2013), where 5 mol% of water decreased T_g by a comparable amount.

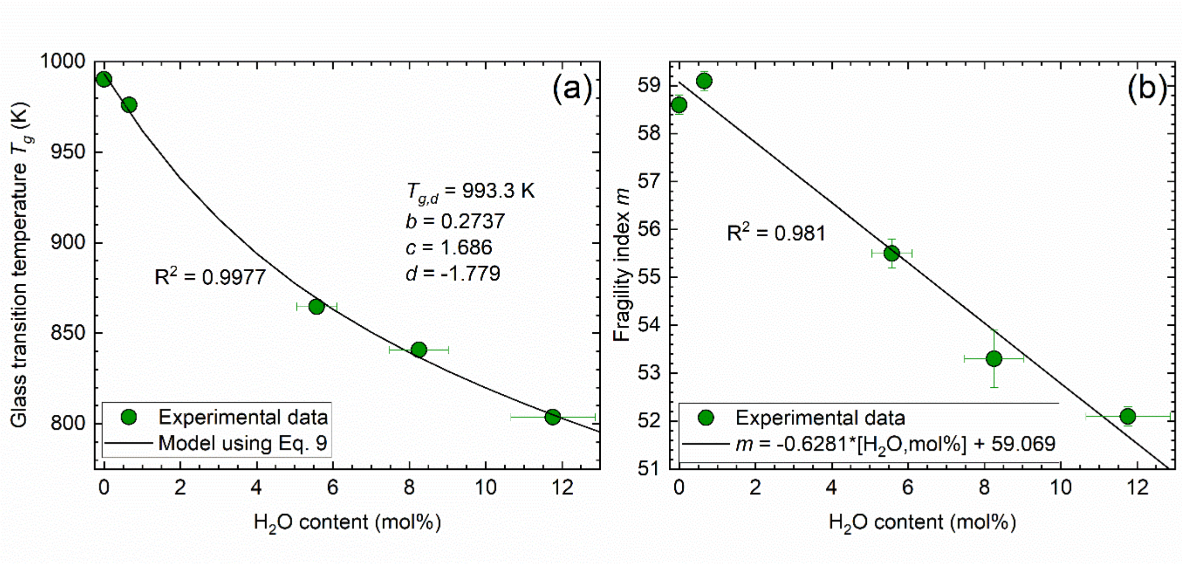

Figure 10. Parameterization of (a) glass transition temperature T_g (model from Eq. 11, Langhammer et al. 2021) and (b) fragility index (m) of hydrous peridotite melts, as a function of their water content. Fit parameters and coefficient of determination R^2 are reported on each graph. Whenever absent, error bars are smaller than the depicted symbols.

Subsequently, we parameterized T_g as a function of the molar water content according to Eq. 11 (Langhammer et al., 2021):

$$T_g(x_{H2O}) = w_1 T_{g,H2O} + w_2 T_{g,d} + c w_1 w_2 \left(T_{g,d} - T_{g,H2O}\right) + d w_1 w_2^2 \left(T_{g,d} - T_{g,H2O}\right) \qquad (11)$$

with (Eq. 12)

$$w_1 = \frac{x_{H2O}}{b(100 - x_{H2O}) + x_{H2O}} \qquad \text{and} \qquad w_2 = \frac{b(100 - x_{H2O})}{b(100 - x_{H2O}) + x_{H2O}} \qquad (12)$$

where X_{H2O} is the mol% of dissolved water, $T_{g,d}$ is the glass transition temperature of the anhydrous composition and $T_{g,H2O}$ is the glass transition temperature of pure water equal to 136 K (Kohl et al., 2005). Note that *b*, *c* and *d* are fitting parameters. As for fragility indices, we linearly fit BLS-derived *m* (Eq. 3 and Tab. 2) as a function of water content. The results of these procedures are summarized in Figure 11: the combination of the MYEGA equation (Eq. 1) with the description of $T_g(H_2O)$ (Eq. 11) and $m(H_2O)$ (linear parameterization in Figure 10-b) enables the modelling of the viscosity of hydrous peridotite melts as a function of temperature and dissolved water content. We provide a viscosity calculator in the Supplementary Material.

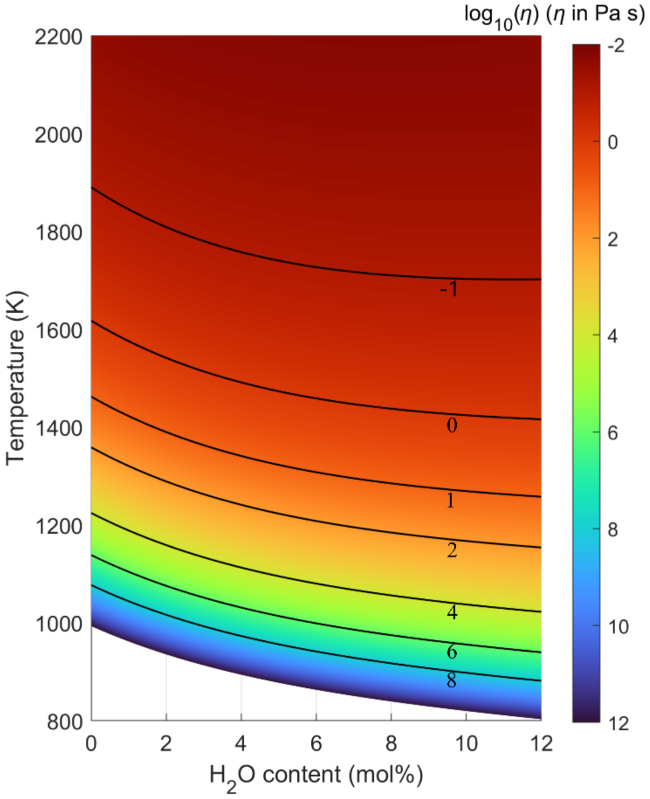

Figure 11. Viscosity of hydrous peridotite melts as a function of temperature and H_2O content. Contour lines are labeled with the respective value of log η.

4.3. *Implications for Earth Science*

Highly ultramafic (peridotite) melts are expected to have formed during the magma ocean stage in the Earth's early history, and may be generated in the present-day deep mantle. Although data on supercooled peridotite liquids at ambient pressure presented in this study are not directly applicable to natural melts, they allow for a more robust extrapolation in the super-liquidus temperature range.

In the current deep mantle, highly ultramafic melts are produced by dehydration melting at the 660-km discontinuity due to the ringwoodite to bridgmanite + ferropericlase phase transitions (Schmandt et al., 2014). These melts are expected to be ultramafic and iron-enriched (Nakajima et al., 2019). The FeO_{tot} in the melts can reach 20 – 30 mol.% because of the high partitioning coefficient of Fe/Mg between melt and solids, while the water content can reach about 20 – 50 wt.% (Fei, 2021; Ghosh and Schmidt, 2014; Nakajima et al., 2019). Although the pressure conditions for the 660-km discontinuity (about 23 GPa) are much higher than the experimental conditions in this study (ambient pressure), the pressure effect on melt viscosity is relatively small (Xie et al., 2021, 2020). Thus, the viscosity of hydrous melt at high pressure is expected to be lowered by more than two orders of magnitude compared to dry peridotite melt. Such a reduction in melt viscosity may further enhance horizontal flow, leading to slab stagnation at the bottom of the mantle transition zone as imaged seismologically (Fukao and Obayashi, 2013). On the other hand, melt at the 660-km discontinuity is gravitationally unstable because of its low density compared to the mantle transition zone (Fei, 2021; Nakajima et al., 2019). Its low viscosity may enhance the upwelling of the melt, which returns water from the subducting slabs back to the mantle transition zone.

In the early history of the Earth, the mantle is expected to have experienced a large degree of melting during accretion and later, after the Moon-forming giant impact, potentially forming a series of terrestrial magma oceans composed of peridotite melt (e.g., Nakajima and Stevenson, 2015). Our results are relevant to the solidification process in a hydrous magma ocean under a dense steam atmosphere. With increasing solid fractions during the cooling of the magma ocean, the crystallized solids and remaining melt could form a homogeneously-distributed mush-like phase if the melt viscosity is relatively high. However, the water-induced reduction of melt viscosity accelerates the segregation of melt from solid by gravity, promoting compositional layering within the planet's interior. On the other hand, it is important to point out that even a significant amount of water (e.g., 10 mol% at 2000 K) has very small effect on viscosity at temperatures > 1800 K (Figure 11). In such case, the physical effects of degassing and/or melting point depression may have greater importance on magma ocean dynamics than the absolute value of viscosity.

Finally, our data shed some light on the effect of water on polymerization in extremely depolymerized melts. While the dissolution of water in polymerized melts depolymerizes them (e.g., Stolper, 1982; Zotov and Keppler, 1998), the depolymerizing effect of water decreases with increasing depolymerization (e.g., Mysen, 2014; Mysen and Cody, 2005; Xue and Kanzaki, 2004 and references therein). As a result, there is an ongoing debate over whether the addition of water to extremely depolymerized melt has no or little depolymerizing effect, or whether it can polymerize the melt. A recent Raman study on these peridotite glasses indicated a shift of the high-wavenumber envelope to higher wavenumbers with increasing water content, suggesting polymerization (Bondar et al., 2022). However, a subsequent FTIR study demonstrated that the proportions of (Mg,Ca)OH and (Si,Al)OH species remain constant over a wide range of water contents, suggesting a negligible effect of water on polymerization (Bondar et al., 2023). The present study favors the latter hypothesis since clear decreases in viscosity and glass transition temperature with increasing water contents are observed for this set of peridotite glasses.

5. Conclusions

Overcoming their strong tendency towards crystallization and degassing, we measured the viscosity of anhydrous and hydrous peridotite melts by conventional viscometry, conventional calorimetry, and flash calorimetry. We demonstrate that a combination of these techniques with Brillouin spectroscopy enables the reliable description of melt viscosity between at least 10^{12} and 10^{-1} Pa s. With $m > 50$, peridotites are among the most fragile natural melts; their viscosity exhibits a clear dependence on FeO_{tot}, H_2O and, to a lesser extent, SiO_2 content and iron oxidation state.

The addition of dissolved water leads to a marked and parallel reduction of both T_g and m, which can substantially affect flow behavior at high and intermediate viscosity. We compared our results with predictions from empirical models of volcanic melt viscosity: among long-established and more recent ones, the recently developed neural-network-based model (Langhammer et al., 2022) performed best. We also provide a calculator to derive the viscosity of peridotite melts as a function of temperature and dissolved water content.

Acknowledgements

Danilo Di Genova acknowledges the funding from the European Research Council (ERC) under the European Union’s Horizon Europe research and innovation programme (NANOVOLC, ERC Consolidator Grant – No. 101044772). Danilo Di Genova acknowledges the Deutsche Forschungsgemeinschaft (DFG) project DI 2751/2-1. Alessio Zandonà acknowledges the DFG for funding his research through the Walter Benjamin Program, project no. 448961237, ZA 1188/1-1 and ZA 1188/2-1; he is also grateful to Dr. Mathieu Allix for granting access to the containerless melting facility available at CNRS CEMHTI in Orléans (France). Joachim Deubener acknowledges the funding of DFG under grant number DE 598/33-1. Tomoo Katsura acknowledges t the funding of DFG under grant number KA/3434/12-1.

References

Al-Mukadam, R., Di Genova, D., Bornhöft, H., Deubener, J., 2020. High rate calorimetry derived viscosity of oxide melts prone to crystallization. J. Non. Cryst. Solids 536.

Al-Mukadam, R., Götz, I.K., Stolpe, M., Deubener, J., 2021a. Viscosity of metallic glass-forming liquids based on Zr by fast-scanning calorimetry. Acta Mater. 221, 117370. https://doi.org/10.1016/j.actamat.2021.117370

Al-Mukadam, R., Zandona, A., Deubener, J., 2021b. Kinetic fragility of pure TeO2 glass. J. Non. Cryst. Solids 554, 1–6. https://doi.org/10.1016/j.jnoncrysol.2020.120595

Angell, C.A., 1995. Formation of Glasses from Liquids and Biopolymers. Science (80-.). 267, 1924–1935. https://doi.org/10.1126/science.267.5206.1924

Armstrong, J.T., 1991. Quantitative Elemental Analysis of Individual Microparticles with Electron Beam Instruments, in: Heinrich, K.F.J., Newbury, D.E. (Eds.), Electron Probe Quantitation. Springer US, Boston, MA, pp. 261–315. https://doi.org/10.1007/978-1-4899-2617-3_15

Behrens, H., Bauer, U., Reinsch, S., Kiefer, P., Müller, R., Deubener, J., 2018. Structural relaxation mechanisms in hydrous sodium borosilicate glasses. J. Non. Cryst. Solids 497, 30–39. https://doi.org/10.1016/j.jnoncrysol.2018.05.025

Bondar, D., 2023. Speciation of water and molar absorptivities of near-infrared OH- and H2O bands in hydrous peridotitic glasses quenched by a novel rapid-quench multi-anvil technique. University of Bayreuth.

Bondar, D., Fei, H., Withers, A.C., Ishii, T., Chanyshev, A., Katsura, T., 2021. A simplified rapid-quench multi-anvil technique. Rev. Sci. Instrum. 92. https://doi.org/10.1063/5.0062525

Bondar, D., Fei, H., Withers, A.C., Katsura, T., 2020. A rapid-quench technique for multi-anvil high-pressure-temperature experiments. Rev. Sci. Instrum. 91. https://doi.org/10.1063/5.0005936

Bondar, D., Withers, A.C., Whittington, A.G., Fei, H., Katsura, T., 2023. Dissolution mechanisms of water in depolymerized silicate (peridotitic) glasses based on infrared spectroscopy. Geochim. Cosmochim. Acta 342, 45–61. https://doi.org/https://doi.org/10.1016/j.gca.2022.11.029

Bondar, D., Zandona, A., Withers, A.C., Fei, H., Di Genova, D., Miyajima, N., Katsura, T., 2022. Rapid-quenching of high-pressure depolymerized hydrous silicate (peridotitic) glasses. J. Non. Cryst. Solids 578. https://doi.org/10.1016/j.jnoncrysol.2021.121347

Bouhifd, M.A., Richet, P., Besson, P., Roskosz, M., Ingrin, J., 2004. Redox state, microstructure and viscosity of a partially crystallized basalt melt. Earth Planet. Sci. Lett. 218, 31–44. https://doi.org/10.1016/s0012-821x(03)00641-1

Bouhifd, M.A., Whittington, A.G., Withers, A.C., Richet, P., 2013. Heat capacities of hydrous silicate glasses and liquids. Chem. Geol. 346, 125–134. https://doi.org/10.1016/j.chemgeo.2012.10.026

Cassetta, M., Di Genova, D., Zanatta, M., Ballaran, T.B., Kurnosov, A., Giarola, M., Mariotto, G., 2021. Estimating the viscosity of volcanic melts from the vibrational properties of their parental glasses. Sci. Rep. https://doi.org/10.1038/s41598-021-92407-5

Cassidy, M., Manga, M., Cashman, K. V., Bachmann, O., 2018. Controls on explosive-effusive volcanic eruption styles. Nat. Commun. 9, 2839. https://doi.org/10.1038/s41467-018-05293-3

Chevrel, M.O., Giordano, D., Potuzak, M., Courtial, P., Dingwell, D.B., 2013. Physical properties of CaAl2Si2O8-CaMgSi2O6-FeO-Fe2O3 melts: Analogues for extra-terrestrial basalt. Chem. Geol. 346, 93–105. https://doi.org/10.1016/j.chemgeo.2012.09.004

Cooney, T.F., Sharma, S.K., 1990. Structure of glasses in the systems Mg2SiO4-Fe2SiO4, Mn2SiO4-Fe2SiO4, Mg2SiO4-CaMgSiO4, and Mn2SiO4-CaMnSiO4. J. Non. Cryst. Solids 122, 10–32. https://doi.org/https://doi.org/10.1016/0022-3093(90)90220-G

Cukierman, M., Uhlmann, D.R., 1974. Effects of Iron Oxidation State on Viscosity, Lunar Composition 15555. J. Geophys. Res. 79, 1594–1598. https://doi.org/10.1029/JB079i011p01594

Di Genova, D., Brooker, R.A., Mader, H.M., Drewitt, J.W.E.E., Longo, A., Deubener, J., Neuville, D.R., Fanara, S., Shebanova, O., Anzellini, S., Arzilli, F., Bamber, E.C.E.C.E.C., Hennet, L., La Spina, G., Miyajima, N., Deubener, J., La Spina, G., 2020a. In situ observation of nanolite growth in volcanic melt: A driving force for explosive eruptions. Sci. Adv. 6. https://doi.org/10.1126/sciadv.abb0413

Di Genova, D., Cimarelli, C., Hess, K.-U., Dingwell, D.B., 2016a. An advanced rotational rheometer system for extremely fluid liquids up to 1273 K and applications to alkali carbonate melts. Am. Mineral. 101, 953–959. https://doi.org/10.2138/am-2016-5537CCBYNCND

Di Genova, D., Hess, K.-U., Chevrel, M.O., Dingwell, D.B., 2016b. Models for the estimation of Fe3+/Fetot. ratio in terrestrial and extra- terrestrial alkali- and iron-rich silicate glasses using Raman spectroscopy. Am. Mineral. 101, 943–952. https://doi.org/10.2138/am-2016-5534CCBYNCND

Di Genova, D., Kolzenburg, S., Wiesmaier, S., Dallanave, E., Neuville, D.R., Hess, K.-U., Dingwell, D.B., 2017a. A chemical tipping point governing mobilization and eruption style of rhyolitic magma. Nature 552, 235–238. https://doi.org/10.1038/nature24488

Di Genova, D., Romano, C., Alletti, M., Misiti, V., Scarlato, P., 2014a. The effect of CO2 and H2O on Etna and Fondo Riccio (Phlegrean Fields) liquid viscosity, glass transition temperature and heat capacity. Chem. Geol. 377, 72–86. https://doi.org/10.1016/j.chemgeo.2014.04.001

Di Genova, D., Romano, C., Giordano, D., Alletti, M., 2014b. Heat capacity, configurational heat capacity and fragility of hydrous magmas. Geochim. Cosmochim. Acta 142, 314–333. https://doi.org/10.1016/j.gca.2014.07.012

Di Genova, D., Sicola, S., Romano, C., Vona, A., Fanara, S., Spina, L., 2017b. Effect of iron and nanolites on Raman spectra of volcanic glasses: reassessment of existing strategies to estimate the water content. Chem. Geol. 475, 76–86. https://doi.org/10.1016/j.chemgeo.2017.10.035

Di Genova, D., Vasseur, J., Hess, K.-U., Neuville, D.R., Dingwell, D.B., 2017c. Effect of oxygen fugacity on the glass transition, viscosity and structure of silica- and iron-rich magmatic melts. J. Non. Cryst. Solids 470, 78–85. https://doi.org/10.1016/j.jnoncrysol.2017.05.013

Di Genova, D., Zandona, A., Deubener, J., 2020b. Unravelling the effect of nano-heterogeneity on the viscosity of silicate melts: Implications for glass manufacturing and volcanic eruptions. J. Non. Cryst. Solids 545, 120248. https://doi.org/10.1016/j.jnoncrysol.2020.120248

Dingwell, D.B., Courtial, P., Giordano, D., Nichols, A.R.L., 2004. Viscosity of peridotite liquid. Earth Planet. Sci. Lett. 226, 127–138. https://doi.org/10.1016/j.epsl.2004.07.017

Dingwell, D.B., Hess, K.-U., Wilding, M.C., Brooker, R.A., Di Genova, D., Drewitt, J.W.E., Wilson, M., Weidendorfer, D., 2022. The glass transition and the non-Arrhenian viscosity of carbonate melts. Am. Mineral. 107, 1053–1064. https://doi.org/10.2138/am-2021-7752

Dobson, D.P., Jones, A.P., Rabe, R., Sekine, T., Kurita, K., Taniguchi, T., Kondo, T., Kato, T., Shimomura, O., Urakawa, S., 1996. In-situ measurement of viscosity and density of carbonate melts at high pressure. Earth Planet. Sci. Lett. 143, 207–215. https://doi.org/10.1016/0012-821X(96)00139-2

Douglas, R.W., Armstrong, W.L., Edward, J.., Hall, D., 1965. A penetration viscometer. Glas. Technol. 52–55.

Durben, D.J., McMillan, P.F., Wolf, G.H., 1993. Raman study of the high-pressure behavior of forsterite (Mg2SiO4) crystal and glass. Am. Mineral. 78, 1143–1148.

Fei, H., 2021. Water Content of the Dehydration Melting Layer in the Topmost Lower Mantle. Geophys. Res. Lett. 48, e2020GL090973. https://doi.org/https://doi.org/10.1029/2020GL090973

Fukao, Y., Obayashi, M., 2013. Subducted slabs stagnant above, penetrating through, and trapped below the 660 km discontinuity. J. Geophys. Res. Solid Earth 118, 5920–5938. https://doi.org/https://doi.org/10.1002/2013JB010466

Ghosh, S., Schmidt, M.W., 2014. Melting of phase D in the lower mantle and implications for recycling and storage of H2O in the deep mantle. Geochim. Cosmochim. Acta 145, 72–88. https://doi.org/https://doi.org/10.1016/j.gca.2014.06.025

Giordano, D., Russell, J.K., Dingwell, D.B., 2008. Viscosity of magmatic liquids: A model. Earth Planet. Sci. Lett. 271, 123–134. https://doi.org/10.1016/j.epsl.2008.03.038

Gonnermann, H.M., Manga, M., 2013. Chapter 4: Dynamics of magma ascent in the volcanic conduit, in: Fagents, S.A., Gregg, T.K.P., Lopes, R.M.C.E. (Eds.), Modeling Volcanic Processes: The Physics and Mathematics of Volcanism. Cambridge University Press, pp. 55–84. https://doi.org/10.1017/CBO9781139021562.004

Hagy, H.E., 1963. Experimental Evaluation of Beam-Bending Method of Determining Glass Viscosities in the Range 108 to 1015 Poises. J. Am. Ceram. Soc. 46, 93–97. https://doi.org/https://doi.org/10.1111/j.1151-2916.1963.tb11684.x

Hennet, L., Cristiglio, V., Kozaily, J., Pozdnyakova, I., Fischer, H.E., Bytchkov, a., Drewitt, J.W.E., Leydier, M., Thiaudière, D., Gruner, S., Brassamin, S., Zanghi, D., Cuello, G.J., Koza, M., Magazù, S., Greaves, G.N., Price, D.L., 2011. Aerodynamic levitation and laser heating: Eur. Phys. J. Spec. Top. 196, 151–165. https://doi.org/10.1140/epjst/e2011-01425-0

Hui, H., Zhang, Y., 2007. Toward a general viscosity equation for natural anhydrous and hydrous silicate melts. Geochim. Cosmochim. Acta 71, 403–416. https://doi.org/10.1016/j.gca.2006.09.003

Ishibashi, H., Sato, H., 2007. Viscosity measurements of subliquidus magmas: Alkali olivine basalt from the Higashi-Matsuura district, Southwest Japan. J. Volcanol. Geotherm. Res. 160, 223–238. https://doi.org/10.1016/j.jvolgeores.2006.10.001

Karato, S., Karki, B., Park, J., 2020. Deep mantle melting, global water circulation and its implications for the stability of the ocean mass. Prog. Earth Planet. Sci. 7, 76. https://doi.org/10.1186/s40645-020-00379-3

Kawamoto, T., Holloway, J.R., 1997. Melting Temperature and Partial Melt Chemistry of H_2O-Saturated Mantle Peridotite to 11 Gigapascals. Science (80-.). 276, 240–243. https://doi.org/10.1126/science.276.5310.240

Keller, J., Krafft, M., 1990. Effusive natrocarbonatite activity of Oldoinyo Lengai, June 1988. Bull. Volcanol. 52, 629–645. https://doi.org/10.1007/BF00301213

Kleest, C., Webb, S.L., Fanara, S., 2020. Rheology of melts from the colli albani volcanic district (Italy): a case study. Contrib. to Mineral. Petrol. 175. https://doi.org/10.1007/s00410-020-01720-1

Kohl, I., Bachmann, L., Mayer, E., Hallbrucker, A., Loerting, T., 2005. Glass transition in hyperquenched water? Nature 435, E1–E1. https://doi.org/10.1038/nature03707

Kolzenburg, S., Di Genova, D., Giordano, D., Hess, K.-U., Dingwell, D.B., 2018. The effect of oxygen fugacity on the rheological evolution of crystallizing basaltic melts. Earth Planet. Sci. Lett. 487, 21–32. https://doi.org/10.1016/j.epsl.2018.01.023

Kono, Y., Kenney-benson, C., Hummer, D., Ohfuji, H., Park, C., Shen, G., Wang, Y., Kavner, A., Manning, C.E., 2014. Ultralow viscosity of carbonate melts at high pressures. Nat. Commun. 2–5. https://doi.org/10.1038/ncomms6091

Langhammer, D., Di Genova, D., Steinle-Neumann, G., 2021. Modelling the viscosity of anhydrous and hydrous volcanic melt. Geochemistry Geophys. Geosystems n/a, e2021GC009918. https://doi.org/https://doi.org/10.1029/2021GC009918

Langhammer, D., Steinle-Neumann, G., Di Genova, D., 2022. Modelling Viscosity of Volcanic Melts with Artificial Neural Networks. Geochemistry Geophys. Geosystems 23. https://doi.org/10.1029/2022GC010673

Li, J., Agee, C.B., 1996. Geochemistry of mantle–core differentiation at high pressure. Nature 381, 686–689. https://doi.org/10.1038/381686a0

Liebske, C., Behrens, H., Holtz, F., Lange, R.A., 2003a. The influence of pressure and composition on the viscocity of andesitic melts. Geochim. Cosmochim. Acta 67, 473–485. https://doi.org/10.1016/S0016-7037(02)01139-0

Liebske, C., Behrens, H., Holtz, F., Lange, R.A., 2003b. The influence of pressure and composition on the viscocity of andesitic melts. Geochim. Cosmochim. Acta 67, 473–485. https://doi.org/10.1016/S0016-7037(02)01139-0

Liebske, C., Schmickler, B., Terasaki, H., Poe, B.T., Suzuki, A., Funakoshi, K., Ando, R., Rubie, D.C., 2005. Viscosity of peridotite liquid up to 13 GPa: Implications for magma ocean viscosities. Earth Planet. Sci. Lett. 240, 589–604. https://doi.org/10.1016/j.epsl.2005.10.004

Lipman, P.W., Mullineaux, D.R., 1981. The 1980 eruptions of Mount St. Helens, Washington, Professional Paper. https://doi.org/10.3133/pp1250

Loughlin, S.C., Vye-Brown, C., Sparks, R.S.J., Brown, S.K., Jenkins, S., 2015. Global volcanic hazards and risk. Cambridge University Press, Cambridge.

Mahood, G.A., Hildreth, W., 1986. Geology of the peralkaline volcano at Pantelleria, Strait of Sicily. Bull. Volcanol. 48, 143–172.

Mancini, M., Sendova, M., Mauro, J.C., 2021. Geometric analysis of the calorimetric glass transition and fragility using constant cooling rate cycles. Int. J. Appl. Glas. Sci. 12, 348–357. https://doi.org/https://doi.org/10.1111/ijag.16073

Mauro, J.C., Loucks, R.J., Gupta, P.K., 2009a. Fictive temperature and the glassy state. J. Am. Ceram. Soc. 92, 75–86. https://doi.org/10.1111/j.1551-2916.2008.02851.x

Mauro, J.C., Yue, Y.Z., Ellison, A.J., Gupta, P.K., Allan, D.C., 2009b. Viscosity of glass-forming liquids. Proc. Natl. Acad. Sci. U. S. A. 106, 19780–4. https://doi.org/10.1073/pnas.0911705106

Meerlender, G., 1974. Viskositäts-Temperaturverhalten des Standardglases I der DGG. Glas. Ber. 47, 1–3.

Mysen, B.O., 2014. Water-melt interaction in hydrous magmatic systems at high temperature and pressure. Prog. Earth Planet. Sci. 1, 4. https://doi.org/10.1186/2197-4284-1-4

Mysen, B.O., Boettcher, A.L., 1975. Melting of a Hydrous Mantle: I. Phase Relations of Natural Peridotite at High Pressures and Temperatures with Controlled Activities of Water, Carbon Dioxide, and Hydrogen. J. Petrol. 16, 520–548. https://doi.org/10.1093/petrology/16.1.520

Mysen, B.O., Cody, G.D., 2005. Solution mechanisms of H2O in depolymerized peralkaline melts. Geochim. Cosmochim. Acta 69, 5557–5566. https://doi.org/10.1016/j.gca.2005.07.020

Nakajima, A., Sakamaki, T., Kawazoe, T., Suzuki, A., 2019. Hydrous magnesium-rich magma genesis at the top of the lower mantle. Sci. Rep. 9, 7420. https://doi.org/10.1038/s41598-019-43949-2

Nakajima, M., Stevenson, D.J., 2015. Melting and mixing states of the Earth's mantle after the Moon-forming impact. Earth Planet. Sci. Lett. 427, 286–295. https://doi.org/https://doi.org/10.1016/j.epsl.2015.06.023

Ohtani, E., 1985. The primodial terrestrial magma ocean and its implication for stratification of the mantle. Phys. Earth Planet. Inter. 38, 70–80. https://doi.org/https://doi.org/10.1016/0031-9201(85)90123-2

Persikov, E.S., 1991. The Viscosity of Magmatic Liquids: Experiment, Generalized Patterns. A Model for Calculation and Prediction. Applications, in: Perchuk, L.L., Kushiro, I. (Eds.), Physical Chemistry of Magmas. Springer New York, New York, NY, pp. 1–40. https://doi.org/10.1007/978-1-4612-3128-8_1

Persikov, E.S., Bukhtiyarov, P.G., Sokol, A.G., 2017. Viscosity of hydrous kimberlite and basaltic melts at high pressures. Russ. Geol. Geophys. 58, 1093–1100. https://doi.org/10.1016/j.rgg.2017.08.005

Pirrung, M., Fischer, C., Buchel, G., Gaupp, R., Lutz, H., Neuffer, F.-O., 2003. Lithofacies succession of maar crater deposits in the Eifel area (Germany). Terra Nov. 15, 125–132.

Prescher, C., McCammon, C., Dubrovinsky, L., 2012. MossA: a program for analyzing energy-domain Mössbauer spectra from conventional and synchrotron sources. J. Appl. Crystallogr. 45, 329–331. https://doi.org/10.1107/S0021889812004979

Richet, P., Lejeune, A.M., Holtz, F., Roux, J., 1996. Water and the viscosity of andesite melts. Chem. Geol. 128, 185–197. https://doi.org/10.1016/0009-2541(95)00172-7

Russell, J.K., Giordano, D., Dingwell, D.B., 2003. High-temperature limits on viscosity of non-Arrhenian silicate melts. Am. Mineral. 88, 1390–1394.

Russell, J.K., Giordano, D., Dingwell, D.B., Hess, K.-U., 2002. Modelling the non-Arrhenian rheology of silicate melts: Numerical considerations. Eur. J. Mineral. 14, 417–427. https://doi.org/10.1127/0935-1221/2002/0014-0417

Scarani, A., Zandona, A., Di Fiore, F., Valdivia, P., Putra, R., Miyajima, N., Bornhöft, H., Vona, A., Deubener, J., Romano, C., Di Genova, D., 2022. A chemical threshold controls nanocrystallization and degassing behaviour in basalt magmas. Commun. Earth Environ. 3. https://doi.org/10.1038/s43247-022-00615-2

Scherer, G.W., 1984. Use of the Adam-Gibbs equation in the analysis of structural relaxation. J. Am. Ceram. Soc. 67, 504–511.

Schmandt, B., Jacobsen, S.D., Becker, T.W., Liu, Z., Dueker, K.G., 2014. Dehydration melting at the top of the lower mantle. Science (80-.). 344, 1265–1268. https://doi.org/10.1126/science.1253358

Sigurdsson, H., Carey, S., 1989. Plinian and co-ignimbrite tephra fall from the 1815 eruption of Tambora volcano. Bull. Volcanol. 51, 243–270. https://doi.org/10.1007/BF01073515

Sigurdsson, H., Cashdollar, S., Sparks, R.S.J., 1982. The Eruption of Vesuvius in A. D. 79: Reconstruction from Historical and Volcanological Evidence. Am. J. Archaeol. 86, 39–51. https://doi.org/10.2307/504292

Sinmyo, R., Nakajima, Y., McCammon, C.A., Miyajima, N., Petitgirard, S., Myhill, R., Dubrovinsky, L., Frost, D.J., 2019. Effect of Fe3+ on Phase Relations in the Lower Mantle: Implications for Redox Melting in Stagnant Slabs. J. Geophys. Res. Solid Earth 124, 12484–12497. https://doi.org/https://doi.org/10.1029/2019JB017704

Sinogeikin, S., Bass, J., Prakapenka, V., Lakshtanov, D., Shen, G., Sanchez-Valle, C., Rivers, M., 2006. Brillouin spectrometer interfaced with synchrotron radiation for simultaneous x-ray density and acoustic velocity measurements. Rev. Sci. Instrum. 77.

https://doi.org/10.1063/1.2360884

Sossi, P.A., Burnham, A.D., Badro, J., Lanzirotti, A., Newville, M., O'Neill, H.S.C., 2020. Redox state of Earth's magma ocean and its Venus-like early atmosphere. Sci. Adv. 6, eabd1387. https://doi.org/10.1126/sciadv.abd1387

Stabile, P., Sicola, S., Giuli, G., Paris, E., Carroll, M.. R., Deubener, J., Di Genova, D., 2021. The effect of iron and alkali on the nanocrystal-free viscosity of volcanic melts: A combined Raman spectroscopy and DSC study. Chem. Geol. 559, 119991. https://doi.org/10.1016/j.chemgeo.2020.119991

Stagno, V., Stopponi, V., Kono, Y., Manning, C.E., Irifune, T., 2018. Experimental determination of the viscosity of Na 2 CO 3 melt between 1 . 7 and 4 . 6 GPa at 1200 – 1700 ° C : Implications for the rheology of carbonatite magmas in the Earth ' s upper mantle. Chem. Geol. 501, 19–25. https://doi.org/10.1016/j.chemgeo.2018.09.036

Stolper, E.M., 1982. Water in silicate glasses: An infrared spectroscopic study. Contrib. to Mineral. Petrol. 81, 1-17 LA-English. https://doi.org/10.1007/BF00371154

Taniguchi, H., 1992. Entropy dependence of viscosity and the glass-transition temperature of melts in the system diopside-anorthite. Contrib. to Mineral. Petrol. 109, 295–303. https://doi.org/10.1007/BF00283319

Trots, D.M., Kurnosov, A., Ballaran, T.B., Tkachev, S., Zhuravlev, K., Prakapenka, V., Berkowski, M., Frost, D.J., 2013. The Sm:YAG primary fluorescence pressure scale. J. Geophys. Res. Solid Earth 118, 5805–5813. https://doi.org/10.1002/2013JB010519

Vanden Poel, G., Istrate, D., Magon, A., Mathot, V., 2012. Performance and calibration of the Flash DSC 1, a new, MEMS-based fast scanning calorimeter. J. Therm. Anal. Calorim. 110, 1533–1546. https://doi.org/10.1007/s10973-012-2722-7

Vanden Poel, G., Sargsyan, A., Mathot, V., Assche, G. V, Wurm, A., Schick, C., Krumme, A., Zhou, D., 2011. Recommendation for temperature calibration of fast scanning calorimeters (FsCs) for sample mass and scan rate. Beuth Verlag GmbH, Berlin Adam Met. vivo Vitr. Investig. a nanostructured Coat. Mater. Preclin. study. Int J Nanomedicine 9, 975–984.

Wade, J., Wood, B.J., 2005. Core formation and the oxidation state of the Earth. Earth Planet. Sci. Lett. 236, 78–95. https://doi.org/https://doi.org/10.1016/j.epsl.2005.05.017

Walker, G.P.L., Self, S., Wilson, L., 1984. Tarawera 1886, New Zealand — A basaltic plinian fissure eruption. J. Volcanol. Geotherm. Res. 21, 61–78. https://doi.org/http://dx.doi.org/10.1016/0377-0273(84)90016-7

Weber, J.K.R., 2010. The Containerless Synthesis of Glass. Int. J. Appl. Glas. Sci. 1, 248–256. https://doi.org/https://doi.org/10.1111/j.2041-1294.2010.00026.x

Whitfield, C.H., Brody, E.M., Bassett, W., 1976. Elastic moduli of NaCl by Brillouin scattering at high pressure in a diamond anvil cell. Rev. Sci. Instrum. 47, 942–947.

Whittington, A.G., Hellwig, B.M., Behrens, H., Joachim, B., Stechern, A., Vetere, F., 2009. The viscosity of hydrous dacitic liquids: implications for the rheology of evolving silicic magmas. Bull. Volcanol. 71, 185–199. https://doi.org/10.1007/s00445-008-0217-y

Williams, Q., McMillan, P., Cooney, T.F., 1989. Vibrational spectra of olivine composition glasses: The Mg-Mn join. Phys. Chem. Miner. 16, 352–359. https://doi.org/10.1007/BF00199555

Xie, L., Yoneda, A., Katsura, T., Andrault, D., Tange, Y., Higo, Y., 2021. Direct Viscosity Measurement of Peridotite Melt to Lower-Mantle Conditions: A Further Support for a Fractional Magma-Ocean Solidification at the Top of the Lower Mantle. Geophys. Res. Lett. 48, e2021GL094507. https://doi.org/https://doi.org/10.1029/2021GL094507

Xie, L., Yoneda, A., Yamazaki, D., Manthilake, G., Higo, Y., Tange, Y., Guignot, N., King, A., Scheel, M., Andrault, D., 2020. Formation of bridgmanite-enriched layer at the top lower-mantle during magma ocean solidification. Nat. Commun. 11, 548. https://doi.org/10.1038/s41467-019-14071-8

Xue, X., Kanzaki, M., 2004. Dissolution mechanisms of water in depolymerized silicate melts: Constraints from 1H and 29Si NMR spectroscopy and ab initio calculations. Geochim. Cosmochim. Acta 68, 5027–5057. https://doi.org/https://doi.org/10.1016/j.gca.2004.08.016

Yue, Y.Z., Christiansen, J. deC., Jensen, S.L., 2002. Determination of the fictive temperature for a hyperquenched glass. Chem. Phys. Lett. 357, 20–24. https://doi.org/10.1016/S0009-2614(02)00434-7

Zandona, A., Groß, C.B.M., Rüdinger, B., Deubener, J., 2021. A threshold heating rate for single-stage heat treatments in glass-ceramics containing seed formers. J. Am. Ceram. Soc. 104, 4433–4444. https://doi.org/10.1111/jace.17822

Zandona, A., Moustrous, M., Genevois, C., Véron, E., Canizarès, A., Allix, M., 2022. Glass-forming ability and ZrO2 saturation limits in the magnesium aluminosilicate system. Ceram. Int. 48, 8433–8439. https://doi.org/https://doi.org/10.1016/j.ceramint.2021.12.051

Zandona, A., Patzig, C., Rüdinger, B., Hochrein, O., Deubener, J., 2019. TiO2(B) nanocrystals in Ti-doped lithium aluminosilicate glasses. J. Non-Crystalline Solids X 2, 100025. https://doi.org/10.1016/j.nocx.2019.100025

Zheng, Q., Mauro, J.C., Ellison, A.J., Potuzak, M., Yue, Y., 2011. Universality of the high-temperature viscosity limit of silicate liquids. Phys. Rev. B - Condens. Matter Mater. Phys. 83, 13–15. https://doi.org/10.1103/PhysRevB.83.212202

Zotov, N., Keppler, H., 1998. The influence of water on the structure of hydrous sodium tetrasilicate glasses. Am. Mineral. 83, 823–834. https://doi.org/10.2138/am-1998-7-814